

What did HERA teach us about the structure of the proton?

Amanda Cooper-Sarkar
Oxford University

Abstract

Starting in 2008 the H1 and ZEUS experiments have been combining their data in order to provide the most complete and accurate set of deep-inelastic data as the legacy of HERA. The present review presents these combinations, both published and preliminary, and explores how they have been used to give information on the structure of the proton. The HERAPDF parton distribution functions (PDFs) are presented and compared with other current PDFs and with data from the Tevatron and LHC colliders.

1 Introduction

HERA was an electron(positron)-proton collider located at DESY, Hamburg. It ran in two phases HERA-I from 1992-2001 and HERA-II 2003-2007. Two similar experiments, H1 and ZEUS, took data. In HERA-I running each experiment collected $\sim 100\text{pb}^{-1}$ of e^+p data and $\sim 15\text{pb}^{-1}$ of e^-p data with electron beam energy 27.5 GeV and proton beam energies 820, 920 GeV. In HERA-II running each experiment took $\sim 140\text{pb}^{-1}$ of e^+p data and $\sim 180\text{pb}^{-1}$ of e^-p data with the same electron beam energy and proton beam energies 920 GeV. In addition to this, before the shut-down in 2007, each experiment took $\sim 30\text{pb}^{-1}$ of data with reduced proton beam energies 460, 575 GeV.

Deep inelastic lepton-hadron scattering data has been used both to investigate the theory of the strong interaction and to determine the momentum distributions of the partons within the nucleon. The data from the HERA collider now dominate the world data on deep inelastic scattering since they cover an unprecedented kinematic range: in Q^2 , the (negative of the) invariant mass squared of the virtual exchanged boson, $0.045 < Q^2 < 3 \times 10^{-5}$; in Bjorken x , $6 \times 10^{-7} < x < 0.65$. Furthermore, because the HERA experiments investigated e^+p and e^-p , charge current(CC) and neutral current (NC) scattering, information can be gained on flavour separated up- and down-type quarks and antiquarks and on the gluon- from its role in the scaling violations of perturbative quantum-chromo-dynamics. From 2008, the H1 and ZEUS experiments began to combine their data in order to provide the most complete and accurate set of deep-inelastic data as the legacy of HERA. Data on inclusive cross-sections have been combined for the HERA-I phase of running and a preliminary combination has been made also using the HERA-II data. This latter exercise also includes the data run at lower proton beam energies in 2007. Combination of $F_2^{c\bar{c}}$ data is also underway, and combination of $F_2^{b\bar{b}}$ data and of jet data is foreseen. The HERA collaborations have used these combined data to determine parton distribution functions (PDFs). These analyses had resulted in the HERAPDF sets. The present review concentrates on the information on proton structure which has been gained from these HERA data.

2 Formalism

In the quark parton model deep inelastic lepton-hadron scattering is pictured as in Fig. 1. where l, l' represent leptons (lepton is taken to include antileptons, unless it is necessary to distinguish them), and N represents the nucleon. The associated four vectors are k, k' for the incoming and outgoing leptons respectively, and p for the target (or incoming) nucleon. The process is mediated by the exchange of a virtual vector boson, $V^*(\gamma, W \text{ or } Z)$, with four momentum given by

$$q = k - k'.$$

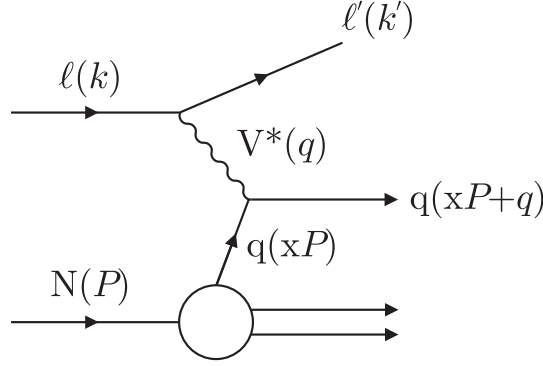


Fig. 1: Schematic diagram of lepton-hadron scattering in the quark-parton model

Various Lorentz invariants are useful in the description of the kinematics of the process:

$$s = (p + k)^2,$$

the centre of mass energy squared for the lp interaction,

$$Q^2 = -q^2,$$

the (negative of) the invariant mass squared of the virtual exchanged boson,

$$x = Q^2/2p \cdot q,$$

the Bjorken x variable, which is interpreted in the quark-parton model as the fraction of the momentum of the incoming nucleon taken by the struck quark, and

$$y = p \cdot q / p \cdot k,$$

which gives a measure of the amount of energy transferred between the lepton and the hadron systems. Note that (ignoring masses),

$$Q^2 = sxy,$$

so that only two of these quantities are independent. Finally the centre of mass of the V^*p system (or equivalently the invariant mass of the final state hadronic system) is often denote by W

$$W^2 = (q + p)^2.$$

Neutral current (NC) deep inelastic scattering is mediated by γ and Z exchange and the NC deep inelastic $e^\pm p$ scattering cross sections can be expressed as

$$\tilde{\sigma}_{NC}^\pm = \frac{Q^4 x}{2\pi\alpha^2 Y_+} \sigma_{NC}^\pm = F_2 \mp \frac{Y_-}{Y_+} xF_3 - \frac{y^2}{Y_+} F_L, \quad (1)$$

where the electromagnetic coupling constant α , the photon propagator and a helicity factor are absorbed in the definition of a reduced cross section $\tilde{\sigma}$, and $Y_\pm = 1 \pm (1 - y)^2$. The structure functions F_2 , F_L and xF_3 are given by

$$\begin{aligned} F_2 &= F_2^\gamma - \kappa_Z v_e \cdot F_2^{\gamma Z} + \kappa_Z^2 (v_e^2 + a_e^2) \cdot F_2^Z, \\ F_L &= F_L^\gamma - \kappa_Z v_e \cdot F_L^{\gamma Z} + \kappa_Z^2 (v_e^2 + a_e^2) \cdot F_L^Z, \\ xF_3 &= \kappa_Z a_e \cdot xF_3^{\gamma Z} - \kappa_Z^2 \cdot 2v_e a_e \cdot xF_3^Z. \end{aligned} \quad (2)$$

where v_e and a_e are the vector and axial-vector weak couplings of the electron and $\kappa_Z(Q^2) = Q^2/[(Q^2 + M_Z^2)(4\sin^2\theta_W \cos^2\theta_W)]$. At low Q^2 , the contribution of Z exchange is negligible and $xF_3 = 0$, $F_2 = F_2^\gamma$, $F_L = F_L^\gamma$ and $\tilde{\sigma} = F_2 - y^2 F_L/Y_+$. The contribution of the term containing the structure function F_L is only significant for large values of y .

In the Quark Parton Model (QPM), $F_L = 0$, and the other strcuture functions are given by

$$\begin{aligned} (F_2^\gamma, F_2^{\gamma Z}, F_2^Z) &= [(e_u^2, 2e_u v_u, v_u^2 + a_u^2)(xU + x\bar{U}) + (e_d^2, 2e_d v_d, v_d^2 + a_d^2)(xD + x\bar{D})], \\ (xF_3^{\gamma Z}, xF_3^Z) &= 2[(e_u a_u, v_u a_u)(xU - x\bar{U}) + (e_d a_d, v_d a_d)(xD - x\bar{D})], \end{aligned} \quad (3)$$

such that at low Q^2

$$F_2^\gamma = [e_u^2(xU + x\bar{U}) + e_d^2(xD + x\bar{D})], \quad (4)$$

where e_u, e_d denote the electric charge of up- or down-type quarks while $v_{u,d}$ and $a_{u,d}$ are the vector and axial-vector weak couplings of the up- or down-type quarks. Here $xU, xD, x\bar{U}$ and $x\bar{D}$ denote the sums of up-type, of down-type and of their anti-quark momentum distributions, respectively. In the QPM these ditributions are functions of Bjorken x only, and not also of Q^2 as they would be in full generality- this is what is meant by Bjorken scaling. Below the b quark mass threshold, these sums are related to the quark distributions as follows

$$xU = xu + xc, \quad x\bar{U} = x\bar{u} + x\bar{c}, \quad xD = xd + xs, \quad x\bar{D} = x\bar{d} + x\bar{s}, \quad (5)$$

where xs and xc are the strange and charm quark distributions. Assuming symmetry between sea quarks and anti-quarks, the valence quark distributions result from

$$xu_v = xU - x\bar{U}, \quad xd_v = xD - x\bar{D}. \quad (6)$$

Charge current (CC) deep inelastic scattering is mediated by W^+ and W^- exchange and the CC deep inelastic $e^\pm p$ scattering cross sections can be expressed as

$$\tilde{\sigma}_{CC}^\pm = \frac{2\pi x}{G_F^2} \left[\frac{M_W^2 + Q^2}{M_W^2} \right]^2 \sigma_{CC}^\pm \quad (7)$$

where analogously to Eq 1,

$$\tilde{\sigma}_{CC}^\pm = \frac{Y_+}{2} W_2^\pm \mp \frac{Y_-}{2} xW_3^\pm - \frac{y^2}{2} W_L^\pm. \quad (8)$$

In the QPM, $W_L^\pm = 0$, and the CC structure functions represent sums and differences of quark and anti-quark-type distributions depending on the charge of the lepton beam:

$$W_2^+ = x\bar{U} + xD, \quad xW_3^+ = xD - x\bar{U}, \quad W_2^- = xU + x\bar{D}, \quad xW_3^- = xU - x\bar{D}. \quad (9)$$

From these equations it follows that

$$\tilde{\sigma}^+ = x\bar{U} + (1-y)^2 xD, \quad \tilde{\sigma}^- = xU + (1-y)^2 x\bar{D}. \quad (10)$$

Therefore the NC and CC measurements may be used to determine the combined sea quark distribution functions, $x\bar{U}$ and $x\bar{D}$, and the valence quark distributions, xu_v and xd_v .

Perturbative QCD extends the formalism of the QPM such that the parton momentum distributions (PDFs) become functions of Q^2 as well as x . However this scaling violation induces only a logarithmic dependence on Q^2 , as described by the DGLAP equations [1–4]. The DGLAP equations are coupled equations for the change of the quark, antiquark and gluon densities as $\ln Q^2$ changes

$$\begin{aligned} \frac{\partial}{\partial \ln Q^2} \begin{pmatrix} q_i(x, Q^2) \\ g(x, Q^2) \end{pmatrix} &= \frac{\alpha_s(Q^2)}{2\pi} \sum_j \int_x^1 \frac{d\xi}{\xi} \\ &\begin{pmatrix} P_{q_i q_j}(\frac{x}{\xi}, \alpha_s(Q^2)) & P_{q_i g}(\frac{x}{\xi}, \alpha_s(Q^2)) \\ P_{g q_j}(\frac{x}{\xi}, \alpha_s(Q^2)) & P_{g g}(\frac{x}{\xi}, \alpha_s(Q^2)) \end{pmatrix} \begin{pmatrix} q_j(\xi, Q^2) \\ g(\xi, Q^2) \end{pmatrix}, \end{aligned} \quad (11)$$

where the q_i, q_j are taken to include both quarks and antiquark distributions. The splitting functions are expanded as power series in the strong coupling α_s ,

$$\begin{aligned} P_{q_i q_j}(z, \alpha_s) &= \delta_{ij} P_{qq}^{(0)}(z) + \frac{\alpha_s}{2\pi} P_{qq}^{(1)}(z) + \dots \\ P_{qg}(z, \alpha_s) &= P_{qg}^{(0)}(z) + \frac{\alpha_s}{2\pi} P_{qg}^{(1)}(z) + \dots \\ P_{gq}(z, \alpha_s) &= P_{gq}^{(0)}(z) + \frac{\alpha_s}{2\pi} P_{gq}^{(1)}(z) + \dots \\ P_{gg}(z, \alpha_s) &= P_{gg}^{(0)}(z) + \frac{\alpha_s}{2\pi} P_{gg}^{(1)}(z) + \dots \end{aligned}$$

and are calculable within pQCD. Thus the gluon momentum distribution influences the quark distributions through its contribution to their scaling violations, and the gluon PDF is determined by analysing the Q^2 dependence of the data.

To leading order in pQCD the equations for the structure functions in terms of the PDFs are still given by the QPM expressions. However beyond leading order a convolution of parton distributions and QCD-calculable coefficient functions is necessary.

$$\frac{F_2(x, Q^2)}{x} = \int \frac{d\xi}{\xi} \left[\sum_i e_i^2 q_i(\xi, Q^2) C_q\left(\frac{x}{\xi}, \alpha_s\right) + \bar{e}^2 g(\xi, Q^2) C_g\left(\frac{x}{\xi}, \alpha_s\right) \right], \quad (12)$$

where, $\bar{e}^2 = \sum_i e_i^2$, and the sums run over all active quark and antiquark flavours. C_q and C_g are the coefficient functions, which may also be expanded as power series in α_s ,

$$\begin{aligned} C_q(z, \alpha_s) &= \delta(1-z) + \frac{\alpha_s}{2\pi} C_q^1(z) + \dots \\ C_g(z, \alpha_s) &= \frac{\alpha_s}{2\pi} C_g^1(z) + \dots \end{aligned}$$

In the QPM the transverse momentum of the partons is assumed to be zero and one of the consequences of this for spin $\frac{1}{2}$ quarks is that the longitudinal structure function ($F_L = F_2 - 2xF_1$) is zero. However this is no longer true beyond leading order, and F_L is given by.

$$\frac{F_L(x, Q^2)}{x} = \frac{\alpha_s}{2\pi} \int_x^1 \frac{d\xi}{\xi} \left[\sum_i e_i^2 \frac{8}{3} \left(\frac{x}{\xi}\right) q_i(\xi, Q^2) + \bar{e}^2 4 \left(\frac{x}{\xi}\right)^2 \left(1 - \frac{x}{\xi}\right) g(\xi, Q^2) \right] \quad (13)$$

Thus the gluon distribution also influences the longitudinal structure function particularly at low x .

3 Data sets

The deep inelastic ep scattering cross sections depend on the centre-of-mass energy s and on two other independent kinematic variables, usually taken to be Q^2 and x . The salient feature of the HERA collider experiments is the possibility to determine the x and Q^2 from the scattered electron, or from the hadronic final state, or using a combination of the two. The choice of the most appropriate kinematic reconstruction method for a given phase space region is based on resolution, measurement accuracy and radiative correction effects and has been optimised differently for the two HERA experiments H1 and ZEUS, as described in the original publications. The use of different reconstruction techniques by the two experiments contributes to improved accuracy when the data sets are combined, since although the detectors were built following similar physics considerations they opted for different technical solutions, both for the calorimetric and the tracking measurements. Thus the experiments can calibrate each other.

Data Set		x Range	Q^2 Range GeV ²	\mathcal{L} pb ⁻¹	e^+/e^-	\sqrt{s}	Reference
H1 svx-mb	95-00	5×10^{-6}	0.02	0.2 12	2.1	e^+p	301-319 [6]
H1 low Q^2	96-00	2×10^{-4}	0.1	12 150	22	e^+p	301-319 [7]
H1 NC	94-97	0.0032	0.65	150 30000	35.6	e^+p	301 [8]
H1 CC	94-97	0.013	0.40	300 15000	35.6	e^+p	301 [8]
H1 NC	98-99	0.0032	0.65	150 30000	16.4	e^-p	319 [9]
H1 CC	98-99	0.013	0.40	300 15000	16.4	e^-p	319 [9]
H1 NC HY	98-99	0.0013	0.01	100 800	16.4	e^-p	319 [10]
H1 NC	99-00	0.0013	0.65	100 30000	65.2	e^+p	319 [10]
H1 CC	99-00	0.013	0.40	300 15000	65.2	e^+p	319 [10]
ZEUS BPC	95	2×10^{-6}	6×10^{-5}	0.11 0.65	1.65	e^+p	301 [11]
ZEUS BPT	97	6×10^{-7}	0.001	0.045 0.65	3.9	e^+p	301 [12]
ZEUS SVX	95	1.2×10^{-5}	0.0019	0.6 17	0.2	e^+p	301 [13]
ZEUS NC	96-97	6×10^{-5}	0.65	2.7 30000	30.0	e^+p	301 [14]
ZEUS CC	94-97	0.015	0.42	280 17000	47.7	e^+p	301 [15]
ZEUS NC	98-99	0.005	0.65	200 30000	15.9	e^-p	319 [16]
ZEUS CC	98-99	0.015	0.42	280 30000	16.4	e^-p	319 [17]
ZEUS NC	99-00	0.005	0.65	200 30000	63.2	e^+p	319 [18]
ZEUS CC	99-00	0.008	0.42	280 17000	60.9	e^+p	319 [19]

Table 1: H1 and ZEUS data sets used for the combination.

3.1 The combined inclusive HERA-I data set

The inclusive cross-sections data collected by each experiment in the HERA-I running period have been combined [5]. A summary of the data used in this analysis is given in Table 1. The NC data cover a wide range in x and Q^2 . The lowest $Q^2 \geq 0.045$ GeV² data come from the measurements of ZEUS using the BPC and BPT [11, 12]. The Q^2 range from 0.2 GeV² to 1.5 GeV² is covered using special HERA runs, in which the interaction vertex position was shifted forward allowing for larger angles of the backward scattered electron to be accepted [6, 13]. The lowest Q^2 for the shifted vertex data was reached using events in which the effective electron beam energy was reduced by initial state radiation [6]. Values of $Q^2 \geq 1.5$ GeV² are measured using the nominal vertex settings. For $Q^2 \leq 10$ GeV², the cross section is very high and the data were collected using dedicated trigger setups [6, 14]. The highest accuracy of the cross-section measurement is achieved for $10 \leq Q^2 \leq 100$ GeV² [7, 14]. For $Q^2 \geq 100$ GeV², the statistical uncertainty of the data becomes relatively large. The high Q^2 data included here were collected with positron [8, 10, 14, 18] and with electron [9, 16] beams. The CC data for e^+p and e^-p scattering cover the range $300 \leq Q^2 \leq 30000$ GeV² [8, 10, 15, 17, 19].

The full details of the combination procedure are given in ref [5]. The combination of the data sets uses the χ^2 minimisation method described in [6]. The χ^2 function takes into account the correlated systematic uncertainties for the H1 and ZEUS cross-section measurements. Global normalisations of the data sets are split into an overall normalisation uncertainty of 0.5%, common to all data sets, due to uncertainties of higher order corrections to the Bethe-Heitler process used for the luminosity calculation, and experimental uncertainties which are treated as correlated systematic sources. Some sources of point-to-point correlated uncertainties are common for CC and NC data and for several data sets of the same experiment. The systematic uncertainties were treated as independent between H1 and ZEUS apart from the 0.5% overall normalisation uncertainty. All the NC and CC cross-section data from H1 and ZEUS are combined in one simultaneous minimisation. Therefore resulting shifts of the correlated systematic uncertainties propagate coherently to both CC and NC data.

There are in total 110 sources of correlated systematic uncertainty, including global normalisations, characterising the separate data sets. None of these systematic sources shifts by more than 2σ of the nominal value in the averaging procedure. The absolute normalisation of the combined data set is to a large extent defined by the most precise measurements of NC e^+p cross-section in the $10 \leq Q^2 \leq 100$ GeV² kinematic range. Here the H1 [7] and ZEUS [14] results move towards each other and the other data sets follow this adjustment.

The influence of several correlated systematic uncertainties is reduced significantly for the averaged result. For example, the uncertainty due to the H1 LAr calorimeter energy scale is halved while the uncertainty due to the ZEUS photoproduction background is reduced by a factor of 3. There are two main reasons for these significant reductions. Since H1 and ZEUS use different reconstruction methods similar systematic sources influence the measured cross section differently as a function of x and Q^2 . Therefore, requiring the cross sections to agree at all x and Q^2 constrains the systematics efficiently. In addition, for some regions of the phase space, one of the two experiments has superior precision compared to the other. For these regions, the less precise measurement is fitted to the more precise one, with a simultaneous reduction of the correlated systematic uncertainty. This reduction propagates to the other average points, including those which are based solely on the measurement from the less precise experiment.

In addition to the 110 sources of systematic uncertainty which result from the separate data sets there are three sources of procedural uncertainty deriving from the choices made in the combination. Firstly all systematic uncertainties were treated as multiplicative, this has been varied by treating all sources bar the normalisations as additive, and the difference is used to estimate a procedural systematic error. Secondly, the correlated systematics from H1 and ZEUS were treated as uncorrelated between the experiments, but this may not be completely true due to some similarity of methods. An alternative combination procedure treats 12 sources of similar systematics as correlated. This results in some differences in the result for the photo-production background and the hadronic energy scale and these differences are used to estimate two further procedural systematic errors.

The data averaging procedure results in a set of measurements for each process: the average cross section value at a point i , its relative correlated systematic, relative statistical and relative uncorrelated systematic uncertainties, respectively. The number of degrees of freedom, ndf , is calculated as the difference between the total number of measurements and the number of combined data points. The value of χ^2_{\min}/ndf is a measure of the consistency of the data sets.

Tabulated results for the average NC and CC cross sections and the structure function F_2 together with statistical, uncorrelated systematic and procedural uncertainties are given in ref [5]. The total integrated luminosity of the combined data set corresponds to about 200 pb^{-1} for e^+p and 30 pb^{-1} for e^-p . In total 1402 data points are combined to 741 cross-section measurements. The data show good consistency, with $\chi^2/ndf = 636.5/656$, and there are no tensions between the input data sets.

For $Q^2 \geq 100 \text{ GeV}^2$ the precision of the H1 and ZEUS measurements is about equal and thus the systematic uncertainties are reduced uniformly. For $2.5 \leq Q^2 < 100 \text{ GeV}^2$ and $Q^2 < 1 \text{ GeV}^2$ the precision is dominated by the H1 [6,7] and ZEUS [12] measurements, respectively. Therefore the overall reduction of the uncertainties is smaller, and it is essentially obtained from the reduction of the correlated systematic uncertainty. The total uncertainty of the combined measurement is typically smaller than 2% for $3 < Q^2 < 500 \text{ GeV}^2$ and reaches 1% for $20 < Q^2 < 100 \text{ GeV}^2$. The uncertainties are larger for high inelasticity $y > 0.6$ due to the photoproduction background.

In Fig 2 averaged data are compared to the input H1 and ZEUS data, illustrating the improvement in precision. Because of the reduction in size of the systematic error this improvement is far better than would be expected simply from the rough doubling of statistics which combining the two experiments represents. In Fig 3, the combined NC e^+p data at very low Q^2 are shown. In Fig 4 the NC reduced cross section, for $Q^2 > 1 \text{ GeV}^2$, is shown as a function of Q^2 for the HERA combined e^+p data and for fixed-target data [20,21] across the whole of the measured kinematic plane. The combined NC $e^\pm p$ reduced cross sections are compared in the high- Q^2 region in Fig 5. In Figs 6 and 7 the combined data set is shown for CC scattering at high Q^2 . The HERAPDF1.0 fit, described in Sec. 4, used these data as input. It is superimposed on the data in the kinematic region suitable for the application of perturbative QCD.

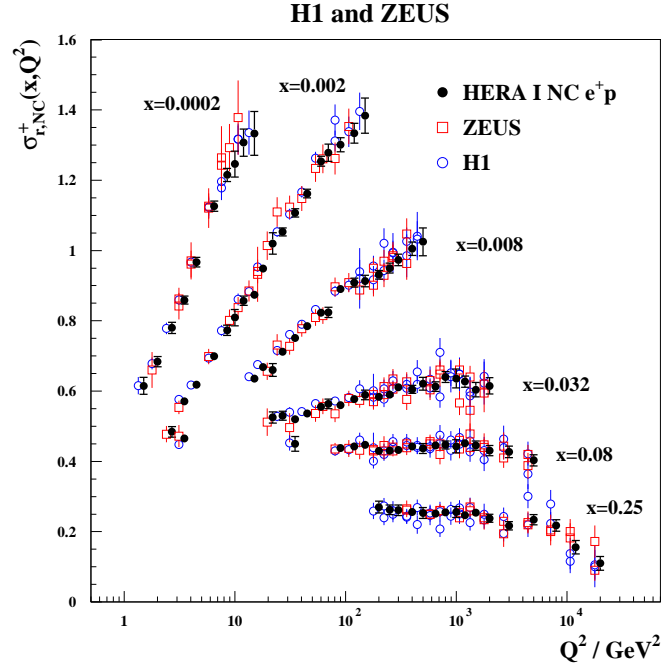


Fig. 2: HERA combined NC e^+p reduced cross section as a function of Q^2 for six x -bins compared to the separate H1 and ZEUS data input to the averaging procedure. The individual measurements are displaced horizontally for a better visibility.

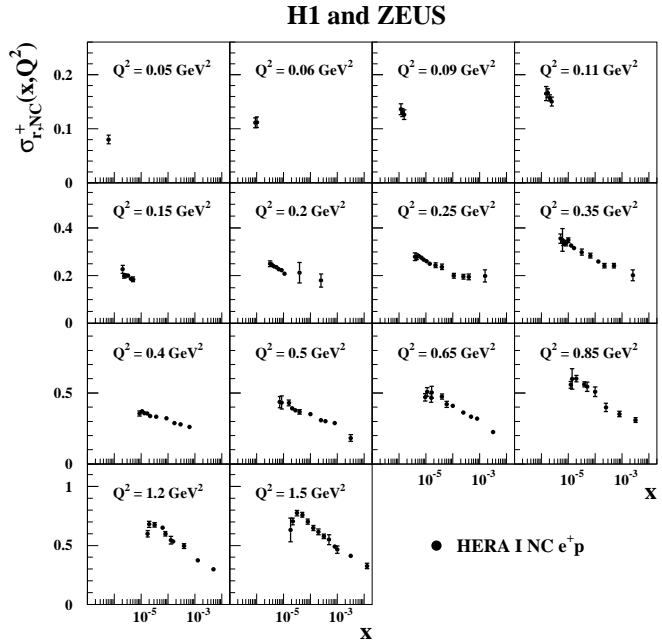


Fig. 3: HERA combined NC e^+p reduced cross section at very low Q^2 .

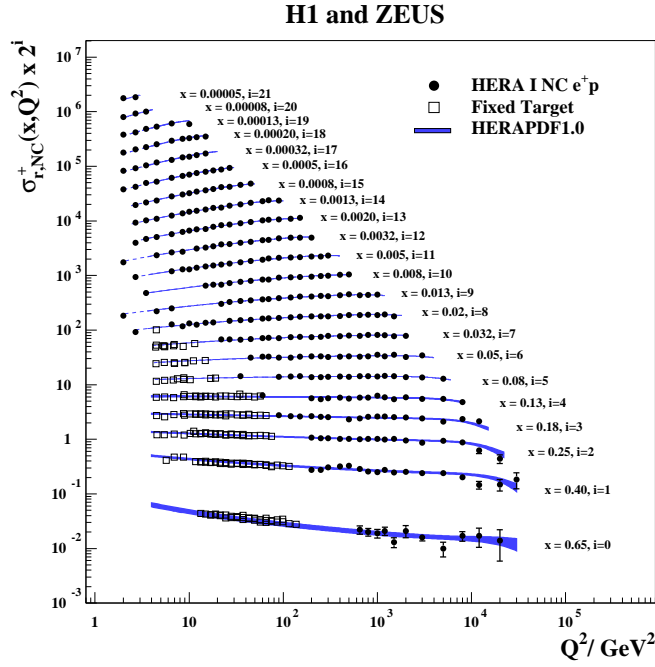


Fig. 4: HERA combined NC e^+p reduced cross section and fixed-target data as a function of Q^2 . The HERAPDF1.0 fit is superimposed. The bands represent the total uncertainty of the fit. The dashed lines are shown for Q^2 values not included in the QCD analysis.

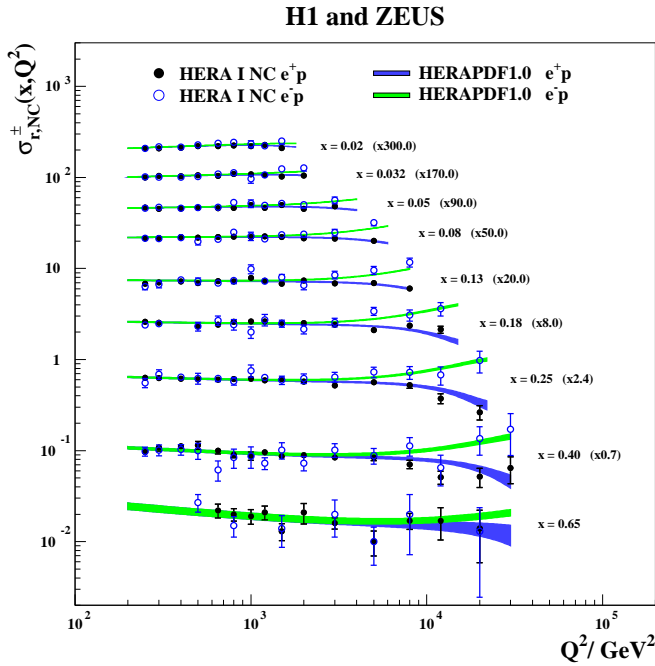


Fig. 5: HERA combined NC $e^\pm p$ reduced cross sections at high Q^2 . The HERAPDF1.0 fit is superimposed. The bands represent the total uncertainty of the fit.

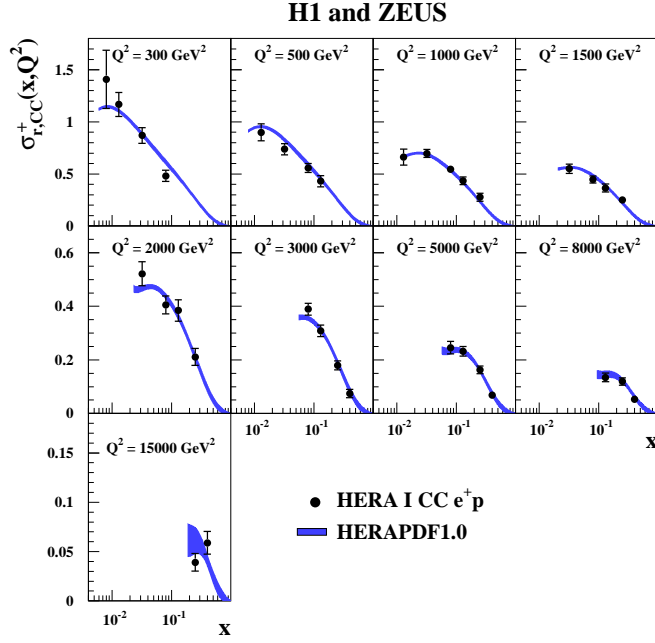


Fig. 6: HERA combined CC e^+p reduced cross section. The HERAPDF1.0 fit is superimposed. The bands represent the total uncertainty of the fit.

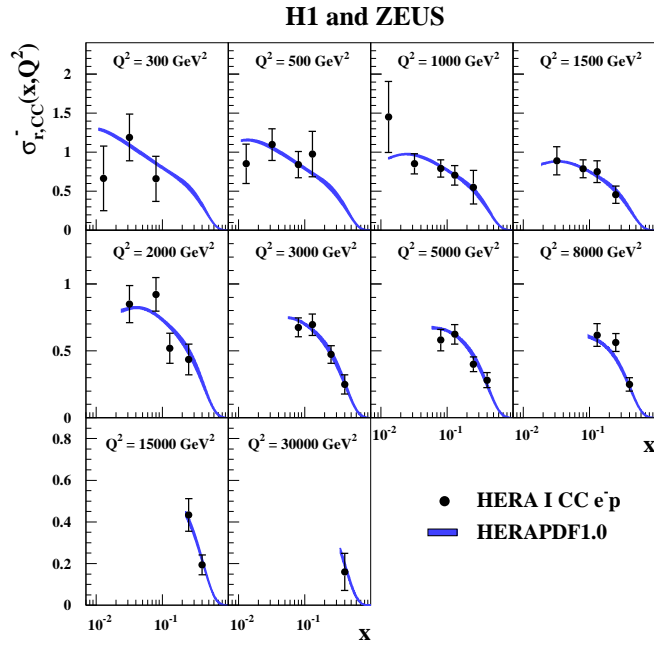


Fig. 7: HERA combined CC e^-p reduced cross section. The HERAPDF1.0 fit is superimposed. The bands represent the total uncertainty of the fit.

New Data Set	Luminosity in pb^{-1}	Reference
CC e^-p 04/06 ZEUS	175	[23]
CC e^-p 04/06 H1	180	[24]
NC e^-p 05/06 ZEUS	170	[25]
NC e^-p 05/06 H1	180	[26]
CC e^+p 06/07 ZEUS	132	[27]
CC e^+p 06/07 H1	149	[24]
NC e^+p 06/07 ZEUS	135	[28]
NC e^+p 06/07 H1	149	[26]

Table 2: Luminosities of the HERA-II data sets.

New Data Set	Luminosity in pb^{-1}	Reference
ZEUS $E_p = 460$ GeV	13.9	[32]
ZEUS $E_p = 575$ GeV	7.1	[32]
ZEUS $E_p = 920$ GeV	45	[32]
H1 $E_p = 460$ GeV	12.4	[31]
H1 $E_p = 575$ GeV	6.2	[31]
H1 $E_p = 920$ GeV	21.6	[31]
H1 $E_p = 460$ GeV	12.2	[34]
H1 $E_p = 575$ GeV	5.9	[34]
H1 $E_p = 920$ GeV	97.6, 5.9	[34]

Table 3: Luminosities of the data sets for the low energy running. The first 6 data sets have already been combined. The final 3 will be combined.

3.2 HERA-II inclusive data sets

The published inclusive data combination does not include the data from the HERA-II running period 2003-2007. These data were collected for both electron and positron beams, polarised both positively and negatively, at $\sqrt{s} = 318$ GeV. The polarised data can be used to measure electroweak parameters [22]. This is beyond the scope of the present review. For investigation of the parton distribution functions these data have been combined into unpolarised cross-sections. Details of the luminosities collected are given in Table 2

A preliminary combination of these data with the HERA-I data has been made [29] using the same χ^2 minimisation method, such that a new set of measurements for each process, NC and CC e^+p and e^-p , results. There are in total 131 sources of correlated systematic uncertainty, characterising the separate data sets, and three sources of procedural uncertainty, plus the overall normalisation uncertainty of 0.5%, as before. These preliminary combined data are shown in Figs. 8- 10. Comparison of these figures with Figs. 5- 7 shows how much the addition of the HERA-II data improves precision at high x and Q^2 . The HERAPDF1.5 fit [30], described in Sec. 4, used these data as input. It is superimposed on the data in the figures.

3.3 F_L data

During the final running period the proton beam ran at three different proton beam energies (920, 575, 460 GeV) and NC e^+p data were collected. These data access high- y and have been used to measure the longitudinal structure function F_L [31, 32]. The luminosities for the input data for the combination are specified in Table 3

The reduced cross-section data from these runs have been combined [33] and the combination is shown in Fig 11. Using these data a combined measurement of F_L can be made [33]. Recall that the NC e^+p reduced cross section is given by, $\tilde{\sigma} = F_2 - y^2 F_L / Y_+$, for $Q^2 \ll M_Z^2$. Since $Q^2 = sxy$ one

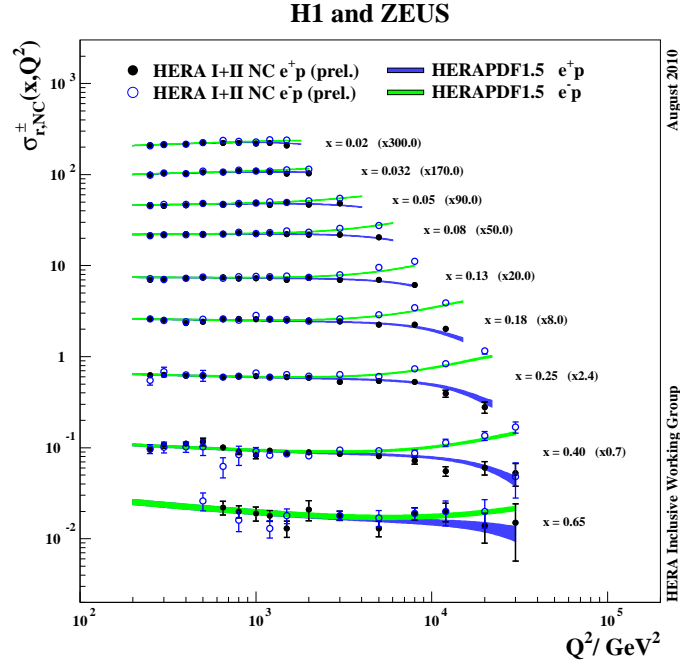


Fig. 8: HERA I+II preliminary combined NC $e^\pm p$ reduced cross sections at high Q^2 . The HERAPDF1.5 fit is superimposed. The bands represent the total uncertainty of the fit.

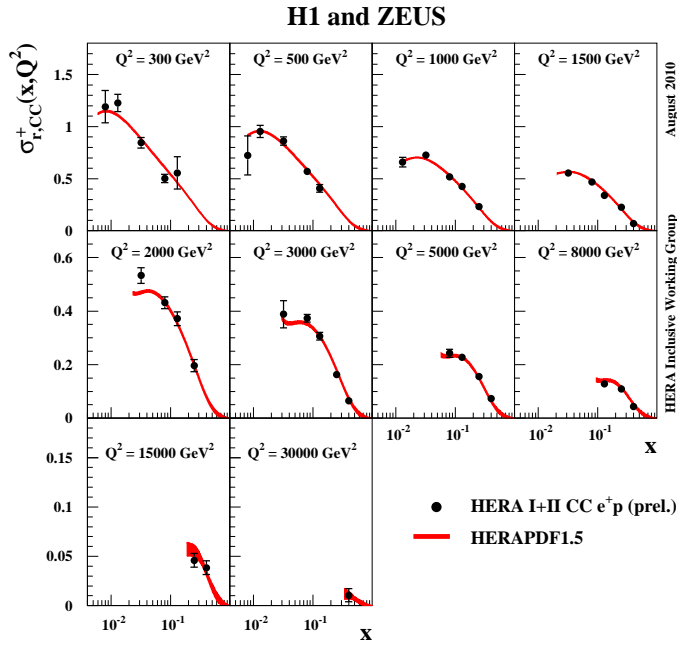


Fig. 9: HERA I+II preliminary combined CC e^+p reduced cross section. The HERAPDF1.5 fit is superimposed. The bands represent the total uncertainty of the fit.

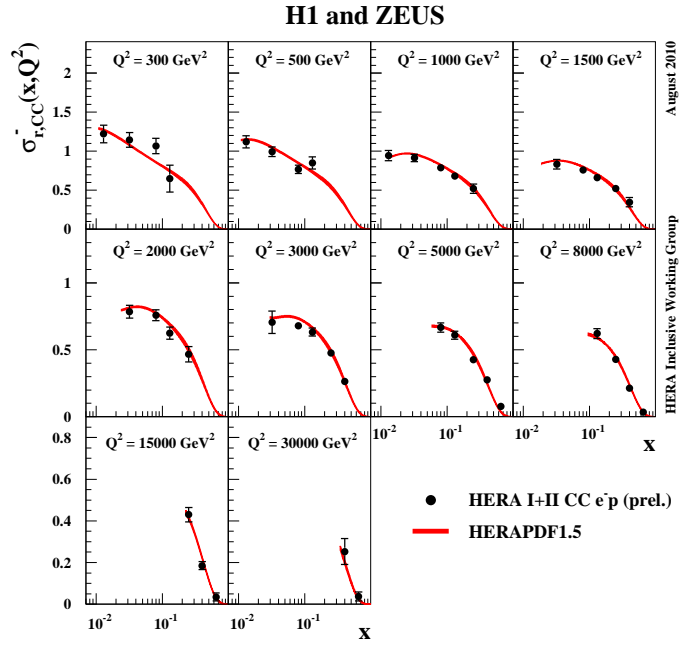


Fig. 10: HERA I+II preliminary combined CC e^-p reduced cross section. The HERAPDF1.5 fit is superimposed. The bands represent the total uncertainty of the fit.

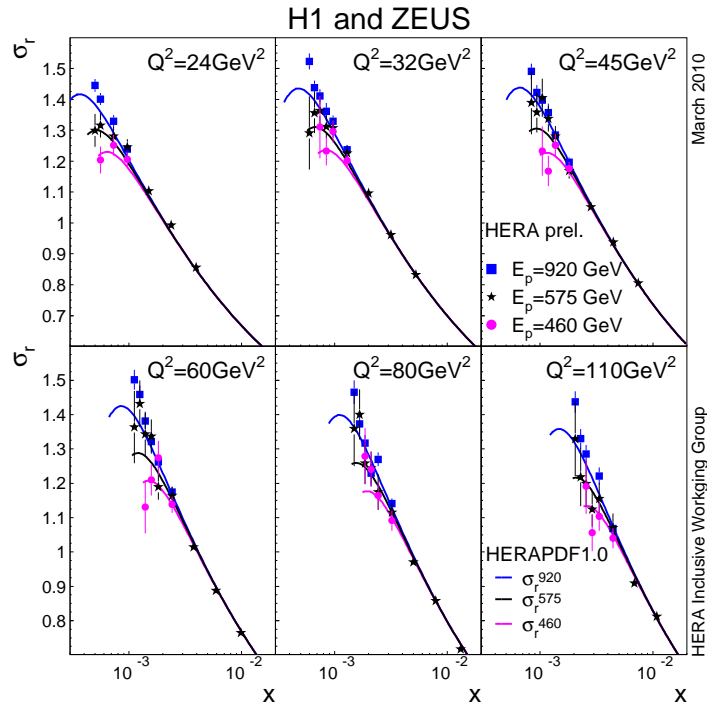


Fig. 11: HERA combined NC e^+p reduced cross sections from running at three different proton beam energies. the predictions of HERAPDF1.0 are superimposed.

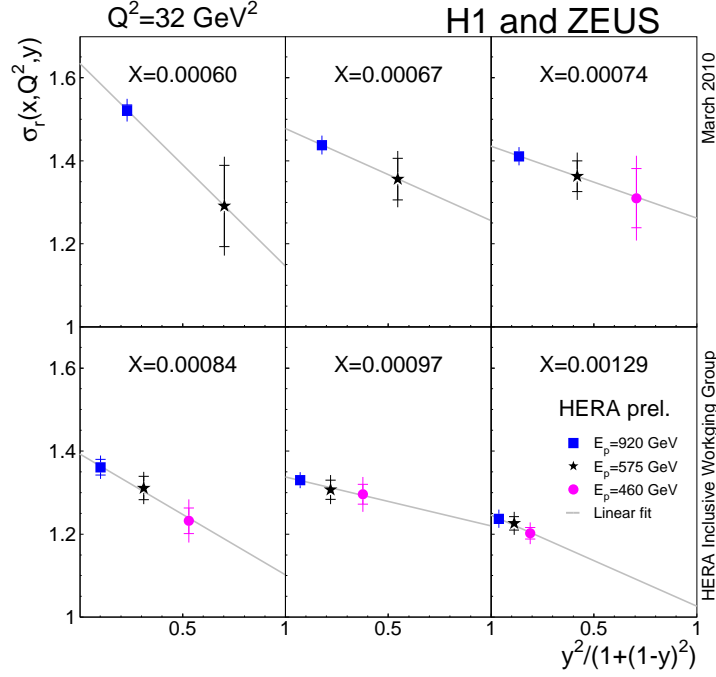


Fig. 12: The slope of $\tilde{\sigma}$ vs $f(y) = y^2/Y_+$ for various x bins at $Q^2 = 32\text{GeV}^2$.

Data Set	Luminosity in pb^{-1}	Reference
D^* 99/00 H1	47	[36]
D^* 04/07 H1	340	[37]
Vtx. 99/00 H1	57.4	[38]
Vtx. 06/07 H1	189	[39]
D^* 98/00 ZEUS	82	[40]
D^* 96/97 ZEUS	37	[41]
D^0, D^\pm 04/05 ZEUS	134	[42]
muons 05 ZEUS	126	[43]

Table 4: Luminosities of the F_2^{cc} data sets.

needs measurements at different s values in order to access different y values for the same x, Q^2 point. The structure function F_L is measured as a slope of a linear fit of $\tilde{\sigma}$ versus $f(y) = y^2/Y_+$, in x, Q^2 bins. Fig 12 shows an example of such a fit, for various x values, at $Q^2 = 32\text{ GeV}^2$. The measured F_L is shown, averaged in x as a function of Q^2 , in Fig 13, with various theoretical predictions superimposed. At low- x , NLO QCD in the DGLAP formalism predicts that this structure function is strongly related to the gluon PDF, see Eqn. 13.

This combination will be updated to include the recently published H1 data, which extend to lower Q^2 [34]. The luminosities used for this extension are given in Table 3 and the F_L measurement from these H1 data is shown in Fig 14.

3.4 $F_2^{c\bar{c}}$ and $F_2^{b\bar{b}}$ data sets

A preliminary combination has been made of data on $F_2^{c\bar{c}}$ [35] from various different methods of tagging charm: using the D^* , using the vertex detectors to see the displaced decay vertex, using direct D_0, D^+ production identified using the vertex detectors, and indentifying semi-leptonic charm decays via muons, also using the vertex detectors. The details of the data sets used in the combination are given in Table 4.

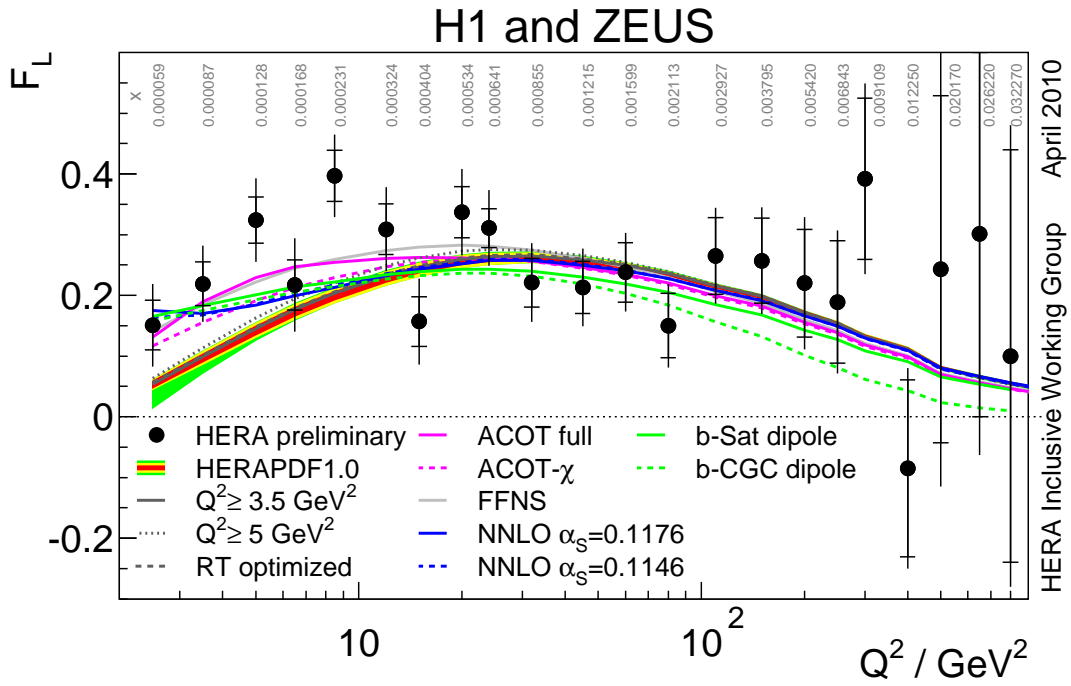


Fig. 13: The HERA combined measurement of F_L averaged in x at a given value of Q^2 .

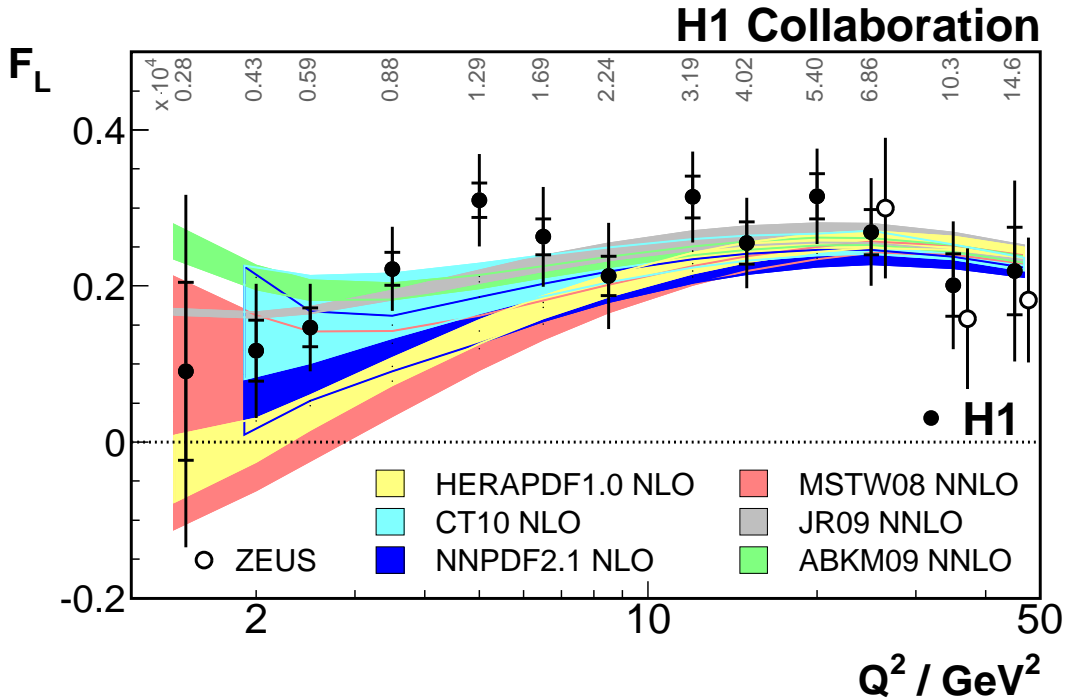


Fig. 14: The H1 2011 measurement of F_L averaged in x at a given value of Q^2 .

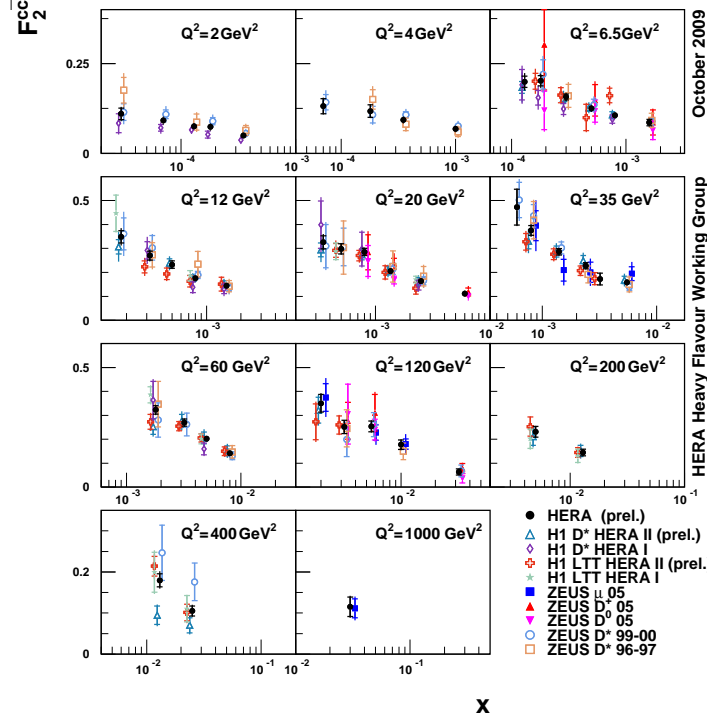


Fig. 15: The HERA combined measurement of $F_2^{c\bar{c}}$ compared to the data sets of H1 and ZEUS used for the combination. these data sets are slightly displaced in x for visibility.

Data Set	Luminosity in pb^{-1}	Reference
High Q^2 norm. inc. jets 96/07 H1	395	[47]
Low Q^2 inc. jets 96/00 H1	43.5	[48]
High Q^2 inc. jets 96/97 ZEUS	38.6	[49]
High Q^2 inc. jets 98/00 ZEUS	82	[50]

Table 5: Luminosities of the jet data sets.

The results of the $F_2^{c\bar{c}}$ combination compared to the separate measurements which went into it are shown in Fig 15. The $F_2^{c\bar{c}}$ combination is shown compared to the predictions of HERAPDF1.0 in Fig. 16

Data on $F_2^{b\bar{b}}$ have not yet been combined. A recent comparison of H1 [44] and ZEUS [45] separate results is shown in Fig. 17.

3.5 Jet data sets

Jet data may also be used to constrain the PDFs. So far H1 and ZEUS jet data have not been combined but some separate H1 and ZEUS jet data sets have been input to the HERAPDF fits in order to exploit their ability to constrain the gluon PDF and to make a determination of the value of $\alpha_s(M_Z)$ simultaneously with the PDF determination [46]. The jet data which have been used are summarised in Table 5 These data are illustrated in Figs 18, 19, 20, 21.

4 Extraction of parton densities

The section discusses how parton momentum densities are extracted from the HERA data¹. There are several PDF fits to different HERA data sets. The HERAPDF1.0 NLO set used only the HERA-I com-

¹Open access code for the HERA PDF fits, and many other useful utilities, are available from the HERAFitter website <http://herafitter.hepforge.org>

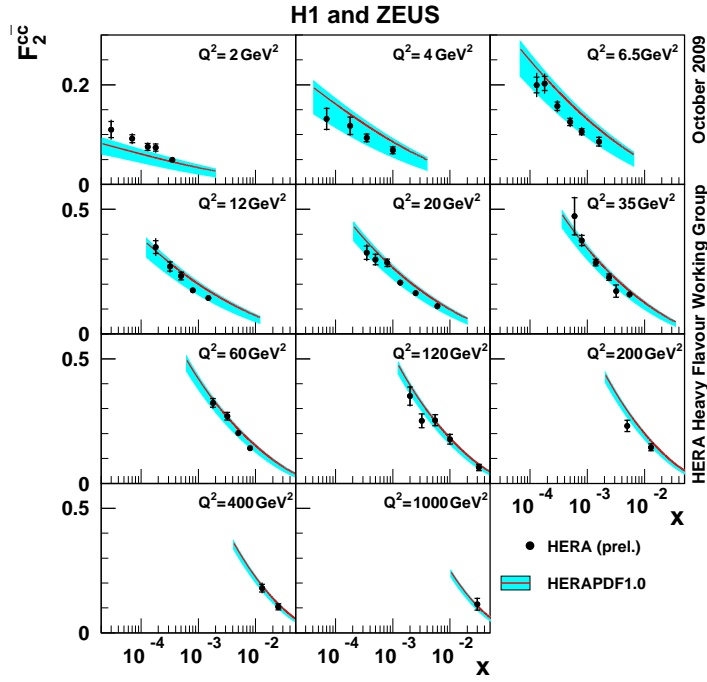


Fig. 16: The HERA combined measurement of $F_2^{c\bar{c}}$ compared to the predictions of HERAPDF1.0

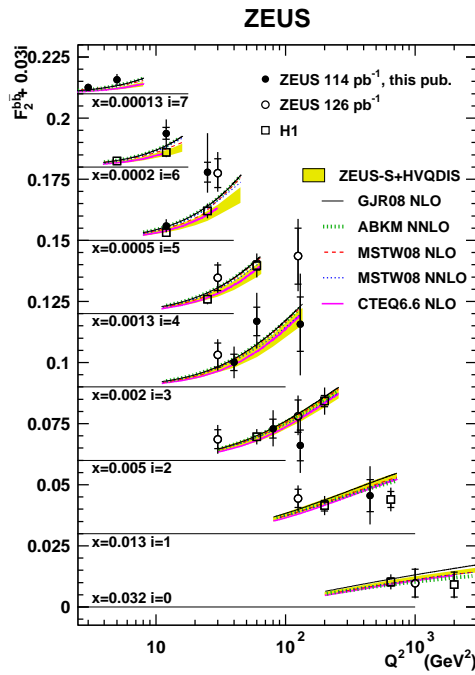


Fig. 17: The H1 and ZEUS measurements of $F_2^{b\bar{b}}$.

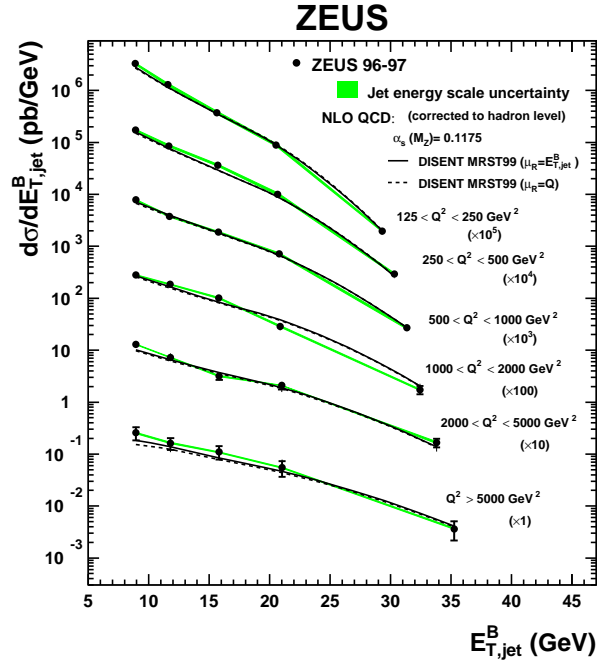


Fig. 18: ZEUS 96/97 measurements of the inclusive jet cross section, as a function of E_T jet in the Breit frame for various Q^2 bins.

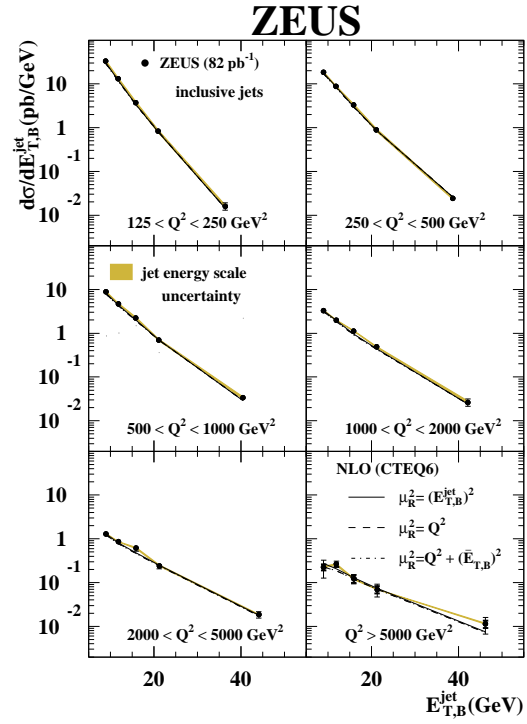


Fig. 19: ZEUS 98/00 measurements of the inclusive jet cross section, as a function of E_T jet in the Breit frame for various Q^2 bins.

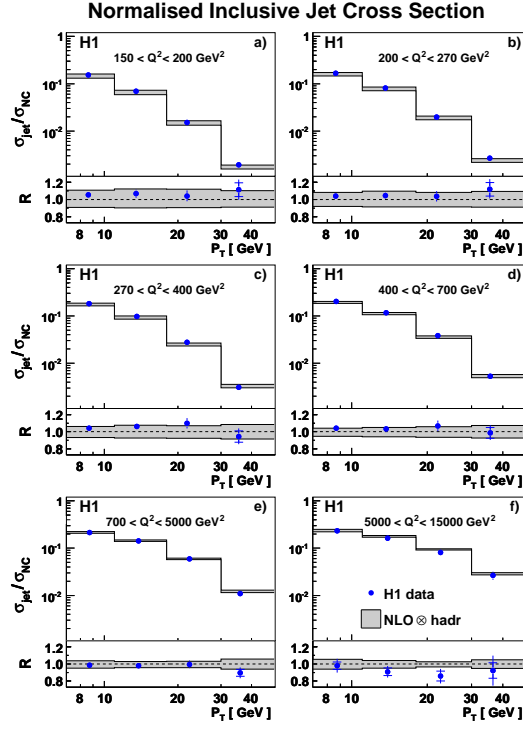


Fig. 20: H1 HERA-I+II measurements of the normalised inclusive jet cross section, as a function of p_T for various Q^2 bins.

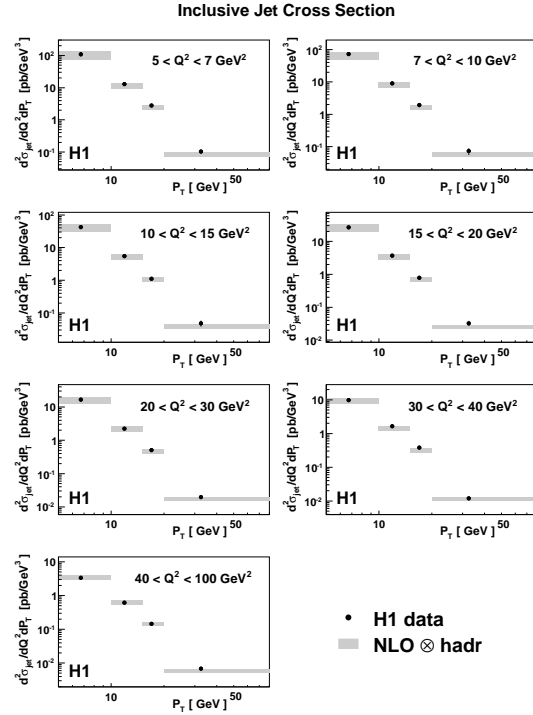


Fig. 21: H1 HERA-I measurements of the low- Q^2 inclusive jet cross section, as a function of p_T jet for various Q^2 bins.

binned data [5]. However there are studies, using the same fit formalism, including the preliminary low-energy combined data [51] and using the preliminary combined F_2^{cc} data [52]. The HERAPDF1.5 NLO set [30] used the HERA-I+II preliminary combined data [29] and the same fit formalism. Studies were also made using the same data but extending the parametrisation HERAPDF1.5f NLO [46]. This extended parametrisation was then used for the HERAPDF1.5 NNLO fit [53]. Subsequent fits also used the extended parametrisation: HERAPDF1.6 NLO fit [46] which included the HERA-I+II inclusive data and separate H1 and ZEUS jet data; HERAPDF1.7 NLO fit [54] which used all the data described in the previous sections (HERA-I+II inclusive data and low energy inclusive data, F_2^{cc} data and H1 and ZEUS jet data sets).

The relationship of the measured cross-sections to the parton distributions, presented in Sec. 1, is not so straightforward beyond LO since the evolved parton distributions must be convoluted with coefficient functions and all types of parton may contribute to a particular structure function through the evolution. However, the simple LO formulae still give a good guide to the major contributions. The cross-sections for NC and CC, e^+ and e^- scattering on protons provide enough information to extract the u and d valence PDFs and the \bar{U} and \bar{D} PDFs, as well as the gluon PDF from scaling violation. Briefly:

- HERA NC e^+ reduced cross-section data at low Q^2 give information on the shape of the sea distribution at low x region, whereas the high Q^2 NC e^+ and e^- cross-sections not only extend the coverage to high x ($x < 0.65$) but also provide information on the valence combination $xF_3 = x(B_u^0 u_v + B_d^0 d_v)$, which is extracted from the difference between the high- Q^2 NC e^+ and e^- cross sections. The x range of the valence measurement is, $0.01 < x < 0.65$.
- HERA CC data gives further information on flavour separation. The e^- cross-section at high- x is u -valence dominated and the e^+ cross-section is d -valence dominated, giving unique information on the d quark. Fixed proton target data are u -quark dominated, and so historically information on the d -quark has been extracted from deuterium target data or from neutrino scattering. However, each of these methods has difficulties. The neutrino data uses heavy isoscalar targets such that uncertain nuclear corrections [55] are necessary. The deuterium target data also needs some nuclear binding corrections [56] and extraction of the d -quark is dependent on the assumption of strong isospin invariance.
- NC data on F_2 have also been used to constrain the gluon distribution. Since the gluon does not couple to the photon it does not enter the expressions for the structure functions at all in the QPM. However, it is constrained by the momentum sum rule, and by the way that gluon to quark-antiquark splitting feeds into the sea distributions (from the P_{qg} term in the DGLAP equations). The shape of the gluon distribution extracted from a DGLAP QCD fit will be correlated with the value of α_s , since an increase in α_s increases the negative contribution from the P_{qq} term but this may be compensated by a positive contribution from the P_{qg} term if the gluon is made harder. Hence, a fixed value of α_s , as determined from independent data, has often been assumed in PDF fits. HERA data are invaluable in constraining the low- x gluon distribution, since at small x QCD evolution becomes gluon dominated and the uncertainties referred to above are reduced. This is because F_2 is essentially given by the singlet sea quark distribution for $x \lesssim 0.01$, and this in turn is driven by the gluon through the P_{qg} term in Eqn. 11. The approximate LO relationship

$$xg(x) \simeq \frac{3\pi}{e^2\alpha_s} \frac{\partial F_2(x/2, Q^2)}{\partial \ln Q^2} \quad (14)$$

illustrates how the gluon distribution depends on the scaling violation of F_2 at low x . Hence in this kinematic region the gluon distribution may be obtained almost directly from the F_2 scaling violation data.

- Jet production data from HERA can give more direct information on the gluon since vector-boson gluon fusion (BGF) to quark-anti-quark pairs makes a significant contribution to final state jet production. Such data has also been input to the PDF fits to constrain the gluon distribution in the x range, $0.01 < x < 0.1$, and to simultaneously determine $\alpha_s(M_Z)$, see Sec. 4.1.5.

- The longitudinal structure function F_L can also give information on the gluon as can be seen from Equation 13. At low x the dominant contribution comes from the gluon and the integral over the gluon distribution approximates to a δ function such that a measurement of $F_L(x, Q^2)$ is almost a direct measurement of the gluon distribution $yg(y, Q^2)$ at $y = 2.5x$ [57]. The heavy quark structure functions $F_2^{c\bar{c}}$ and $F_2^{b\bar{b}}$ may also yield information on the gluon since heavy quarks are generated by the BGF process. However, currently such data are most useful for distinguishing between different schemes for heavy quark production and fixing the value of the heavy quark mass parameters that enter into these schemes, see Sec. 4.1.2

Perturbative QCD predicts the Q^2 evolution of the parton distributions, but not the x dependence. The parton distributions are extracted by performing a direct numerical integration of the DGLAP equations at NLO and NNLO [58]. For most PDF extractions (the notable exception is the NNPDF analysis) a parametrised analytic shape for the parton distributions (valence, sea and gluon) is assumed to be valid at some starting value of $Q^2 = Q_0^2$. This starting value is arbitrary, but should be large enough to ensure that $\alpha_s(Q_0^2)$ is small enough for perturbative calculations to be applicable. For the HERAPDF the value $Q_0^2 = 1.9\text{GeV}^2$ is chosen such that the starting scale is below the charm mass threshold, $Q_0^2 < m_c^2$. Then the DGLAP equations are used to evolve the parton distributions up to higher Q^2 values, where they are convoluted with coefficient functions to make predictions for the structure functions and cross sections. These predictions are then fitted to data to determine the PDF parameters, and thus the shapes of the parton distributions at the starting scale and, through evolution, at any other value of Q^2 .

The QCD evolution is performed using the programme QCDNUM [59]. The HERADF uses the $\overline{\text{MS}}$ renormalisation scheme, with the renormalisation and factorisation scales chosen to be Q^2 . The light quark coefficient functions [60, 61] are calculated using the programme QCDNUM. The heavy quark coefficient functions are calculated in the general-mass variable-flavour-number scheme of [62], with recent modifications and extension to NNLO [63, 64]. (This scheme will be called the RT-VFN scheme). The heavy quark masses for the central fit were chosen to be $m_c = 1.4\text{ GeV}$ and $m_b = 4.75\text{ GeV}$ and the strong coupling constant was fixed to $\alpha_s(M_Z^2) = 0.1176$. These choices are varied to evaluate model uncertainties. The predictions are then fitted to the combined HERA data sets on differential cross sections for NC and CC e^+p and e^-p scattering. A minimum Q^2 cut, $Q_{min}^2 = 3.5\text{ GeV}^2$, was imposed to remain in the kinematic region where perturbative QCD should be applicable. This choice is also varied when evaluating model uncertainties. It is also conventional to apply a minimum cut on W , invariant mass of the hadronic system, to avoid sensitivity to target mass and large- x higher-twist contributions. However the HERA data have $W > 15\text{ GeV}$ and $x < 0.65$, so that no further cuts are necessary.

PDFs were parametrised at the input scale by the generic form

$$xf(x) = Ax^B(1-x)^C(1 + \epsilon\sqrt{x} + Dx + Ex^2). \quad (15)$$

The parametrised PDFs are the gluon distribution xg , the valence quark distributions xu_v, xd_v , and the u -type and d -type anti-quark distributions $x\bar{U}, x\bar{D}$. Here $x\bar{U} = x\bar{u}$, $x\bar{D} = x\bar{d} + x\bar{s}$, at the chosen starting scale. The normalisation parameters, A_g, A_{u_v}, A_{d_v} , are constrained by the quark number sum-rules and momentum sum-rule. The B parameters $B_{\bar{U}}$ and $B_{\bar{D}}$ are set equal, $B_{\bar{U}} = B_{\bar{D}}$, such that there is a single B parameter for the sea distributions. The strange quark distribution is expressed as x -independent fraction, f_s , of the d -type sea, $x\bar{s} = f_s x\bar{D}$ at Q_0^2 . For $f_s = 0.5$ the s and d quark densities would be the same, but the value $f_s = 0.31$ is chosen to be consistent with determinations of this fraction using neutrino-induced di-muon production [65, 66]. This choice is varied when evaluating model uncertainties. The further constraint $A_{\bar{U}} = A_{\bar{D}}(1 - f_s)$, together with the requirement $B_{\bar{U}} = B_{\bar{D}}$, ensures that $x\bar{u} \rightarrow x\bar{d}$ as $x \rightarrow 0$. For the HERAPDF1.0 and 1.5 NLO central fits, the valence B parameters, B_{u_v} and B_{d_v} are also set equal, but this assumption is dropped for fits using the extended paramterisation. The form of the gluon paramterisation is also extended for these latter fits such that a term of the form $A'_g x^{B'_g} (1-x)^{C'_g}$ is subtracted from the standard paramterisation, where $C'_g = 25$ is fixed and A'_g and B'_g are fitted. This allows for the gluon distribution to become negative at low x, Q^2 ,

Variation	Standard Value	Lower Limit	Upper Limit
f_s	0.31	0.23	0.38
m_c [GeV]	1.4	$1.35 (Q_0^2 = 1.8)$	1.65
m_b [GeV]	4.75	4.3	5.0
Q_{min}^2 [GeV ²]	3.5	2.5	5.0
Q_0^2 [GeV ²]	1.9	$1.5 (f_s = 0.29)$	$2.5 (m_c = 1.6, f_s = 0.34)$

Table 6: Standard values of input parameters and the variations considered.

although it does not do so within the kinematic range of the fitted data. The central fit is found by first setting the ϵ , D and E parameters to zero and then varying them, one at a time, the best fit is achieved for $E_{uv} \neq 0$. This is then adopted as standard and the other ϵ , D and E parameters are then varied, one at a time. However these fits do not represent a significant improvement in fit quality for the HERAPDF1.0, 1.5 and 1.7 NLO fits, and thus a central fit with just $E_{uv} \neq 0$ is chosen. For the HERAPDF1.5f, 1.6 and HERAPDF1.5NNLO fit an extra parameter, $D_{uv} \neq 0$ is used. The HERAPDF1.0 and 1.5 NLO fits have 10 parameters, and the 1.5f, 1.6 NLO and 1.5NNLO fits have 14 parameters and the HERAPDF1.7NLO fit has 13 parameters.

The assumptions made in setting the parameters for this central fit are now discussed:

- In common with most PDF fits it is assumed that $q_{sea} = \bar{q}$.
- The HERAPDF parametrizes \bar{U} and \bar{D} separately to allow for the fact that $\bar{u} \neq \bar{d}$ at high x , but the restriction $x\bar{u} \rightarrow x\bar{d}$ as $x \rightarrow 0$ is imposed.
- The strange sea is suppressed. However determinations of the degree of suppression are not very accurate and hence model uncertainty on this fraction is evaluated by allowing the variation, $0.23 < f_s < 0.38$.
- The u -valence and d -valence shapes are parametrized separately, but the form of the parametrization imposes $d_v/u_v = (1-x)^p$ as $x \rightarrow 1$.
- The heavy quarks are treated using a General-Mass-Variable-Flavour Number-Scheme. There is some model uncertainty in the choice of the heavy quark masses. The ranges $1.35 < m_c < 1.65$ GeV and $4.3 < m_b < 5.0$ GeV are considered as model variations. There are also different heavy quark schemes. The ACOT scheme [67] has been used as a cross-check to the Thorne-Roberts scheme.
- All PDF extractions make choices concerning the fitted kinematic region, i.e the minimum values of Q^2 , W^2 , x . These choices can have small systematic effects on the PDF shapes extracted. The choice of Q_{min}^2 is varied in the range $2.5 < Q_{min}^2 < 5.0$.
- The PDFs extracted for $Q^2 \gg Q_0^2$ lose sensitivity to the exact form of the parametrisation at Q_0^2 . However the choices of Q_0^2 and of the form of parametrisation represent a parametrisation uncertainty. The HERAPDF uses the technique of saturation of the χ^2 , increasing the number of parameters systematically until the χ^2/ndf no longer decreases significantly. However, a number of variations on the central fit parametrisation, which have similar fit quality, are considered in order to give an estimate of parametrization uncertainty. The value of Q_0^2 is also varied in the range $1.5 < Q_0^2 < 2.5$ GeV² for the same purpose.

Table 6 summarizes the variations in numerical values considered when evaluating model uncertainties on the HERAPDF. Note that the variations of Q_0^2 and f_s are not independent, since QCD evolution will ensure that the strangeness fraction increases as Q_0^2 increases. The value $f_s = 0.29$ is used for $Q_0^2 = 1.5$ GeV² and the value $f_s = 0.34$ is used for $Q_0^2 = 2.5$ GeV² in order to be consistent with the choice $f_s = 0.31$ at $Q_0^2 = 1.9$ GeV². The variations of Q_0^2 and m_c are also not independent, since $Q_0 < m_c$ is required in the fit programme. Thus when $m_c = 1.35$ GeV, the starting scale used is $Q_0^2 = 1.8$ GeV². Similarly, when $Q_0^2 = 2.5$ GeV² the charm mass used is $m_c = 1.6$ GeV. In practice, the variations of f_s , m_c , m_b , mostly affect the model uncertainty of the $x\bar{s}$, $x\bar{c}$, $x\bar{b}$, quark distributions,

respectively, and have little effect on other parton flavours. The difference between the central fit and the fits corresponding to model variations of m_c , m_b , f_s , Q_{min}^2 are added in quadrature, separately for positive and negative deviations, to represent the model uncertainty of the HERAPDF sets.

The variation in Q_0^2 is regarded as a parametrisation uncertainty, rather than a model uncertainty. The variations of Q_0^2 mostly increase the PDF uncertainties of the sea and gluon at small x . At the starting scale the gluon shape is valence-like, so for the downward variation of the starting scale, $Q_0^2 = 1.5 \text{ GeV}^2$, a gluon parametrisation which explicitly allows for a negative gluon contribution at low x is considered for the 1.0 and 1.5 NLO fits- in all other HERAPDF fits it is already a standard part of the parametrisation. Similarly a parametrisation variation, $B_{u_v} \neq B_{d_v}$, which is standard for the 1.5f, 1.6 and 1.7 NLO and the 1.5NNLO fits, is also allowed for the 1.0 and 1.5 NLO fits. This increases the uncertainties on the valence quarks at low x . Finally, variation of the number of terms in the polynomial $(1 + \epsilon\sqrt{x} + Dx + Ex^2)$ is considered for each fitted parton distribution. In practice only a small number of these variations have significantly different PDF shapes from the central fit, notably: $D_{u_v} \neq 0$ (standard for 1.5f, 1.6 NLO and 1.5NNLO), $D_{\bar{U}} \neq 0$ and $D_{\bar{D}} \neq 0$. These variations mostly increase the PDF uncertainty at high x , but the valence PDFs at low x are also affected because of the constraints of the quark number sum rules. The difference between all these parametrisation variations and the central fit is stored and an envelope representing the maximal deviation at each x value is constructed to represent the parametrisation uncertainty.

The HERAPDF uses a form of the χ^2 specified in ref [5] to perform the fit of the predictions to the HERA data. The consistency of the input data justifies the use of the conventional χ^2 tolerance, $\Delta\chi^2 = 1$, when determining the 68%C.L. experimental uncertainties on the HERAPDF1.0 fit. Modern deep inelastic scattering experiments have very small statistical uncertainties, so that the contribution of correlated systematic uncertainties has become dominant for individual data sets and consideration of the treatment of such errors is essential. However, the HERA data combination has changed this situation. The combination of the H1 and ZEUS data sets has resulted in a data set for NC and CC e^+p and e^-p scattering with correlated systematic uncertainties which are smaller or comparable to the statistical and uncorrelated uncertainties. Thus the central values and experimental uncertainties on the PDFs which are extracted from the combined data are not much dependent on the method of treatment of correlated systematic uncertainties in the fitting procedure. For the HERAPDF1.0(1.5) NLO central fit, the 110(131) systematic uncertainties which result from the ZEUS and H1 data sets are combined in quadrature, and the three sources of uncertainty which result from the combination procedure are treated as correlated by the Offset method [68]. The resulting experimental uncertainties on the PDFs are small. For the HERAPDF1.5f, 1.6, 1.7 NLO fits and the HERAPDF1.5 NNLO fit it was decided to treat the three procedural errors as correlated by the Hessian method [68]. This has a negligible effect on the size of the experimental uncertainties and a small effect on the resulting χ^2 value, see Sec. 4.1.4. The total PDF uncertainty is obtained by adding in quadrature experimental, model and parameterisation uncertainties.

4.1 Results from the HERAPDF fit

4.1.1 HERAPDF1.0

We first discuss results from the published HERAPDF1.0 fit. This fit has a χ^2 per degree of freedom of 574/582. Fig 22 shows summary plots of the HERAPDF1.0 PDFs at $Q^2 = 10 \text{ GeV}^2$.

Figs 23-25 show the HERAPDF1.0 distributions, xu_v, xd_v, xS, xg , as a function of x at $Q^2 = 10, 10000 \text{ GeV}^2$, where $xS = 2x(\bar{U} + \bar{D})$ is the sea PDF. Note that for $Q^2 > m_c^2$, $x\bar{U} = x\bar{u} + x\bar{c}$, and for $Q^2 > m_b^2$, $x\bar{D} = x\bar{d} + x\bar{s} + x\bar{b}$, so that the heavy quarks are included in the sea distributions. The break-up of xS into the flavours $xu_{sea} = 2x\bar{u}$, $xd_{sea} = 2x\bar{d}$, $xs_{sea} = 2x\bar{s}$, $xc_{sea} = 2x\bar{c}$, $xb_{sea} = 2x\bar{b}$ is illustrated so that the relative importance of each flavour at different Q^2 may be assessed. Fractional uncertainty bands are shown below each PDF. The experimental, model and parametrisation uncertainties are shown separately. The model and parametrisation uncertainties are asymmetric. For the sea and

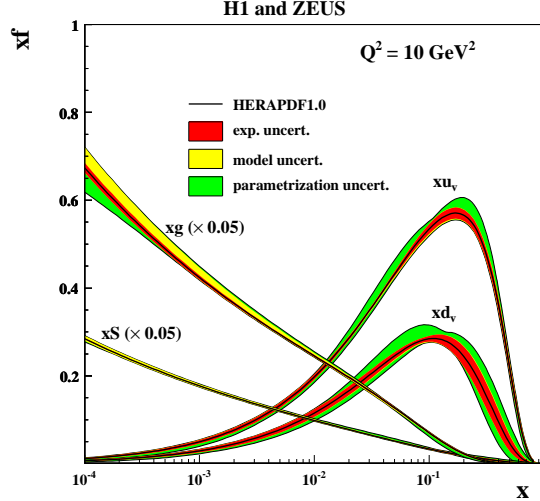


Fig. 22: The parton distribution functions from HERAPDF1.0, $xu_v, xd_v, xs = 2x(\bar{u} + \bar{d}), xg$, at $Q^2 = 10 \text{ GeV}^2$. The experimental, model and parametrisation uncertainties are shown separately. The gluon and sea distributions are scaled down by a factor 20.

gluon distributions, the variations in parametrisation which have non-zero ϵ , D and E affect the large- x region, and the uncertainties arising from the variation of Q_0^2 and Q_{min}^2 affect the small- x region. For the valence distributions the non-zero ϵ , D and E parametrisation uncertainty is important for all x , and is their dominant uncertainty. The total uncertainties at low x decrease with increasing Q^2 due to QCD evolution resulting, for instance, in 2% uncertainties for xg at $Q^2 = 10000 \text{ GeV}^2$ for $x < 0.01$.

The break-up of the PDFs into different flavours is further illustrated in Fig 26, where the quark distributions $x\bar{u}, x\bar{d}, x\bar{c}, x\bar{s}$ are shown at $Q^2 = 10 \text{ GeV}^2$. The u flavour is better constrained than the d flavour because of the dominance of this flavour in all interactions except e^+p CC scattering. The quark distribution $x\bar{s}$ is derived from $x\bar{D}$ through the assumption on the value of f_s , and the uncertainty on $x\bar{s}$ directly reflects the uncertainty on this fraction. The charm PDF, $x\bar{c}$, is strongly related to the gluon density such that it is affected by the same variations which affect the gluon PDF (variation of Q_0^2 and Q_{min}^2) as well as by the variation of m_c . The uncertainty on the bottom PDF, $x\bar{b}$ (not shown), is dominated by the variation of m_b .

The shapes of the gluon and the sea distributions can be compared by considering Figs 23-25. For $Q^2 \gtrsim 10 \text{ GeV}^2$, the gluon density rises dramatically towards low x and this rise increases with increasing Q^2 . This rise is one of the most striking discoveries of HERA. However, at low Q^2 the gluon shape flattens at low x . At $Q^2 = 1.9 \text{ GeV}^2$, the gluon shape becomes valence like and the parametrisation variation which includes a negative gluon term increases the uncertainty on the gluon at low x . However the gluon distribution itself is not negative in the fitted kinematic region.

The uncertainty in the sea distribution is considerably less than that of the gluon distribution. For $Q^2 > 5 \text{ GeV}^2$, the gluon density becomes much larger than the sea density, but for lower Q^2 the sea density continues to rise at low x , whereas the gluon density is suppressed. This may be a signal that the application of the DGLAP NLO formalism for $Q^2 \lesssim 5 \text{ GeV}^2$ is questionable. Kinematically low Q^2 HERA data is also at low x and the DGLAP formalism may be inadequate at low x since it is missing $\ln(1/x)$ resummation terms and possible non-linear effects - see Ref. [69]. Discussion of this topic is beyond the scope of the present review. PDF fits within the DGLAP formalism are successful down to $Q^2 \sim 2 \text{ GeV}^2$ and $x \sim 10^{-4}$ and this is the kinematic region considered in the present review.

4.1.2 Including Heavy Quark data in PDF fits

The HERA combined charm data have been presented in Sec. 3.4. Fig.16 shows the comparison of the HERA combined measurements of $F_2^{c\bar{c}}$ with the predictions of the HERAPDF1.0 fit. These data can of

H1 and ZEUS

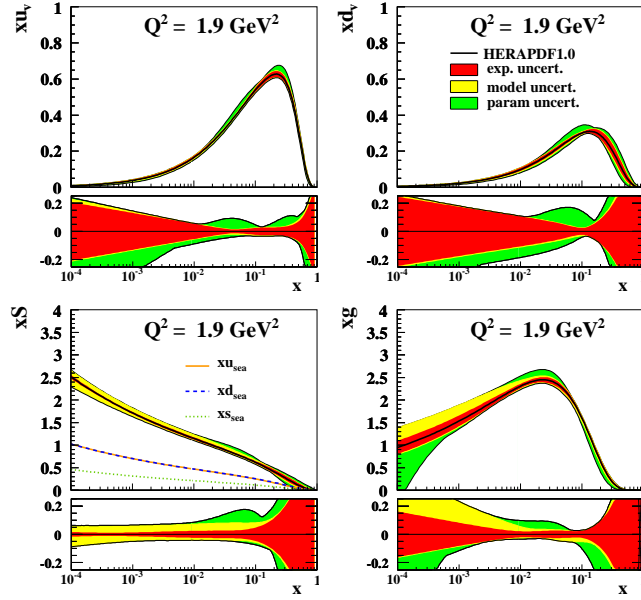


Fig. 23: The parton distribution functions from HERAPDF1.0, $xu_v, xd_v, xS = 2x(\bar{U} + \bar{D}), xg$, at $Q^2 = 1.9 \text{ GeV}^2$. The break-up of the Sea PDF, xS , into the flavours, $xu_{sea} = 2x\bar{u}$, $xd_{sea} = 2x\bar{d}$, $xs_{sea} = 2x\bar{s}$, $xc_{sea} = 2x\bar{c}$ is illustrated. Fractional uncertainty bands are shown below each PDF. The experimental, model and parametrisation uncertainties are shown separately.

H1 and ZEUS

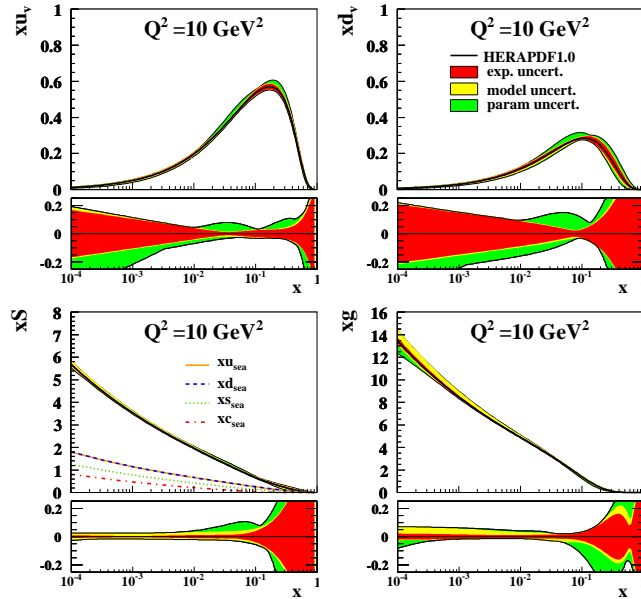


Fig. 24: The parton distribution functions from HERAPDF1.0, $xu_v, xd_v, xS = 2x(\bar{U} + \bar{D}), xg$, at $Q^2 = 10 \text{ GeV}^2$. The break-up of the Sea PDF, xS , into the flavours, $xu_{sea} = 2x\bar{u}$, $xd_{sea} = 2x\bar{d}$, $xs_{sea} = 2x\bar{s}$, $xc_{sea} = 2x\bar{c}$ is illustrated. Fractional uncertainty bands are shown below each PDF. The experimental, model and parametrisation uncertainties are shown separately.

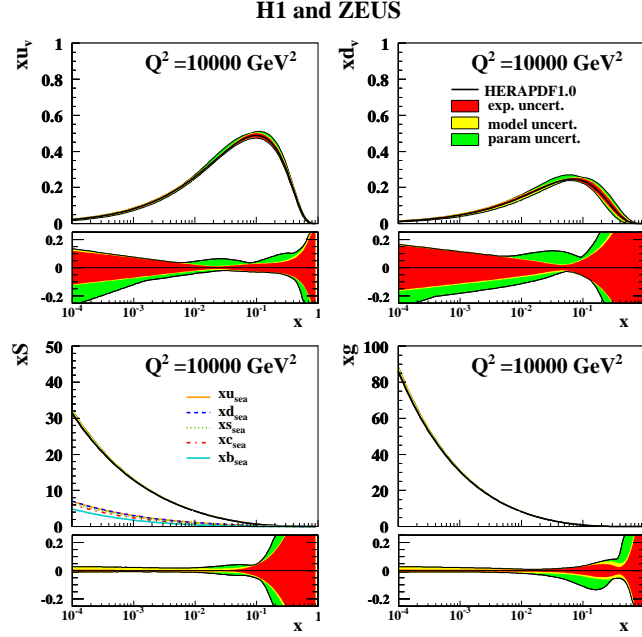


Fig. 25: The parton distribution functions from HERAPDF1.0, xu_v , xd_v , $xS = 2x(\bar{U} + \bar{D})$, xg , at $Q^2 = 10,000 \text{ GeV}^2$. The break-up of the Sea PDF, xS , into the flavours, $xu_{sea} = 2x\bar{u}$, $xd_{sea} = 2x\bar{d}$, $xs_{sea} = 2x\bar{s}$, $xc_{sea} = 2x\bar{c}$, $xb_{sea} = 2x\bar{b}$ is illustrated. Fractional uncertainty bands are shown below each PDF. The experimental, model and parametrisation uncertainties are shown separately.

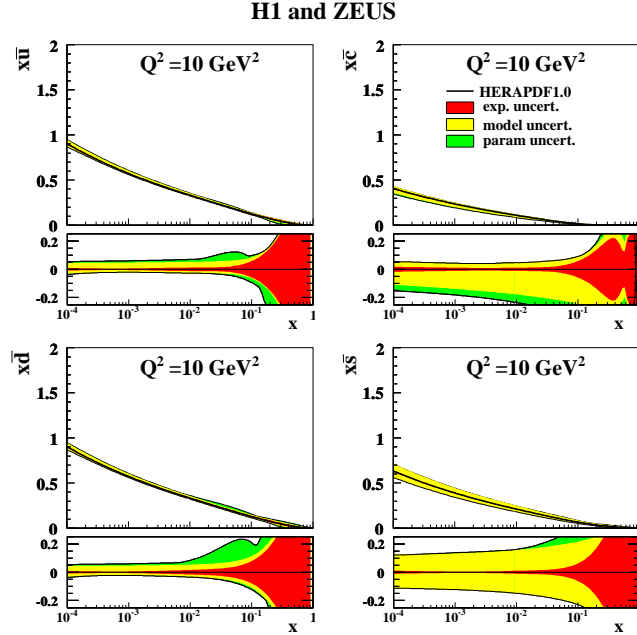


Fig. 26: The parton distribution functions from HERAPDF1.0, $x\bar{u}$, $x\bar{d}$, $x\bar{c}$, $x\bar{s}$ at $Q^2 = 10 \text{ GeV}^2$. Fractional uncertainty bands are shown below each PDF. The experimental, model and parametrisation uncertainties are shown separately.

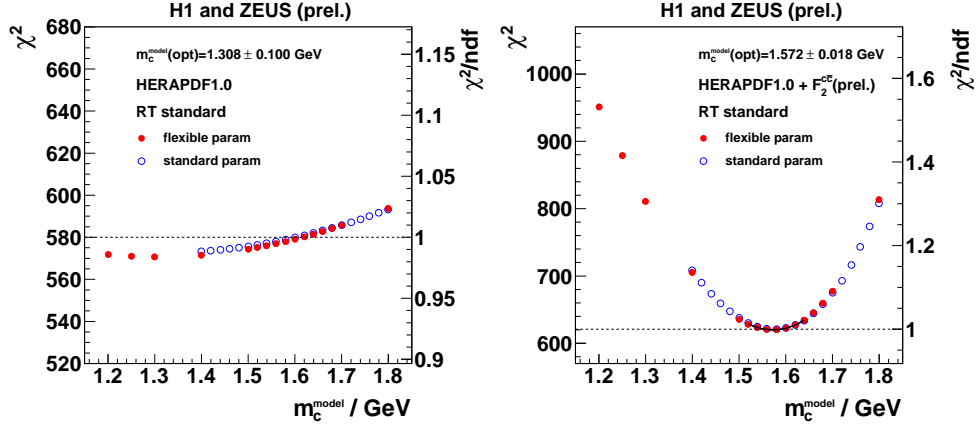


Fig. 27: χ^2 scan vs the charm quark mass m_c for the HERAPDF1.0 fit to just HERA-I inclusive data (left) and a fit which also includes combined HERA F_2^{cc} data (right). Both of these fits use the RT-VFN heavy quark scheme

Scheme	$m_c(\text{minimum})$	$\chi^2/\text{ndp } F_2^{cc}$
RT Standard	$1.58^{+0.02}_{-0.03}$	42.0/41
RT Optimized	$1.46^{+0.02}_{-0.04}$	46.5/41
ACOT-full	$1.58^{+0.03}_{-0.04}$	59.9/41
S-ACOT χ	$1.26^{+0.02}_{-0.04}$	68.5/41
ZM-VFN	$1.68^{+0.06}_{-0.07}$	88.1/41

Table 7: Charm mass parameters and χ^2 values per number of data points (ndp) for fits to F_2^{cc} data using various heavy quark schemes.

course be included in the fit. There are 41 jet data points and, for the preliminary combination, these are provided with uncorrelated systematic errors and a single combined source of correlated error which was treated by the Offset method. The χ^2 for the inclusive data is hardly changed by the addition of the charm data but for the χ^2 for the charm data is very sensitive to the charm mass and the scheme used for heavy flavour treatment [70]. It is found that in order to obtain a good fit using the standard Thorne-Roberts variable Flavour Number Scheme (RT-VFN) [70] it is necessary to increase the standard value of the charm mass. Fig 27 shows a scan of the χ^2 of the HERAPDF1.0 fit to the inclusive HERA-I data vs the charm quark mass parameter entering into the standard RT-VFN scheme. In the same figure a scan for a similar fit to the inclusive HERA-I data plus the combined F_2^{cc} data is shown. The sensitivity of the charm data to the charm quark mass parameter is clear.

However the Standard RT-VFN scheme is not the only possible heavy quark scheme. The fit to HERA-I inclusive plus F_2^{cc} data has been repeated for the Optimized RT-VFN scheme [71], the full ACOT scheme, the S-ACOT- χ scheme [72] and the Zero-Mass Variable Flavour Number Scheme (ZM-VFN) in which light-quark coefficient functions are used for the heavy quarks, which are simply turned on at threshold $Q^2 \sim m_c^2$. Fig. 28 shows the χ^2 scan for these different heavy quark schemes. It can be seen that all schemes, bar the ZM-VFN, give acceptable fits, and that each scheme has its own preferred value of the charm quark mass. These values and the corresponding χ^2 values are given in Table 7. Fig 29 shows these fits compared to the charm data.

Predictions for W^+ , W^- , Z production at the LHC are sensitive to the value of the charm mass and to the heavy quark scheme used, as illustrated in Fig. 28. For any chosen value of the charm mass the spread of predictions for different schemes is $\sim 7\%$. However if each prediction is used at its own favoured value of the charm mass then this spread is reduced to $\sim 2\%$ and, if the disfavoured ZM-VFN is excluded to $\lesssim 1\%$.

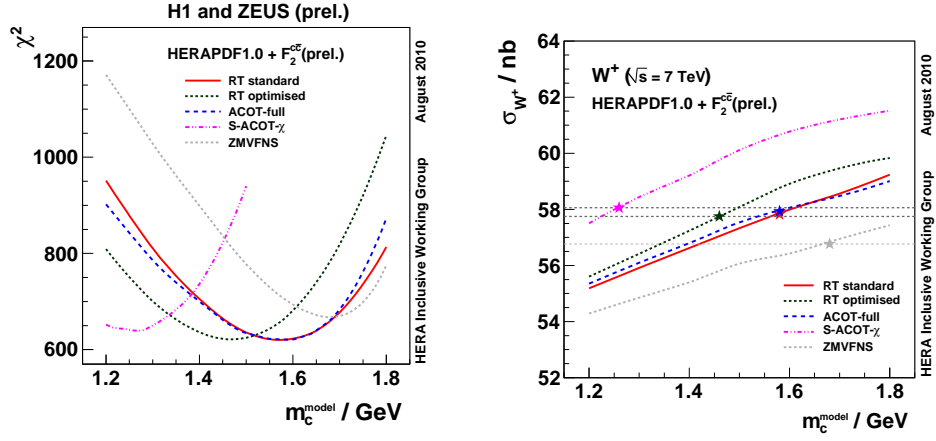


Fig. 28: Left: χ^2 scan vs the charm quark mass m_c for a fit to HERA-I inclusive and F_2^{cc} data for various heavy quark schemes. Right: Predictions for the W^+ cross-section at the LHC (7TeV) for these schemes vs m_c . The value of the charm mass parameter which gives the minimum χ^2 is marked by a star for each scheme.

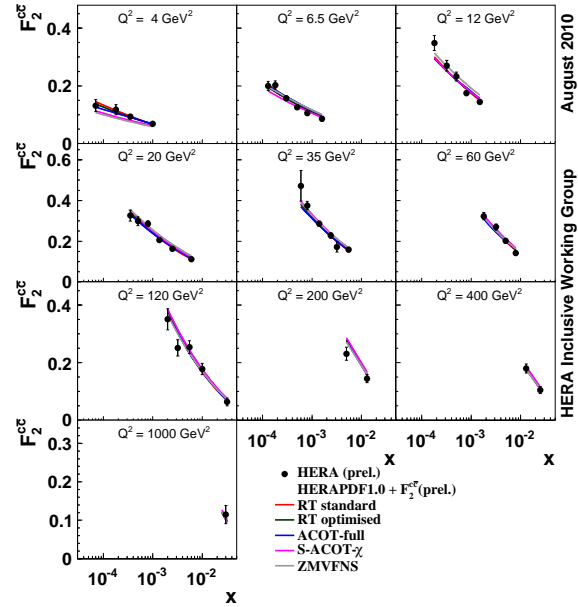


Fig. 29: F_2^{cc} data compared to the predictions of various heavy quark schemes, within the HERAPDF fit formalism.

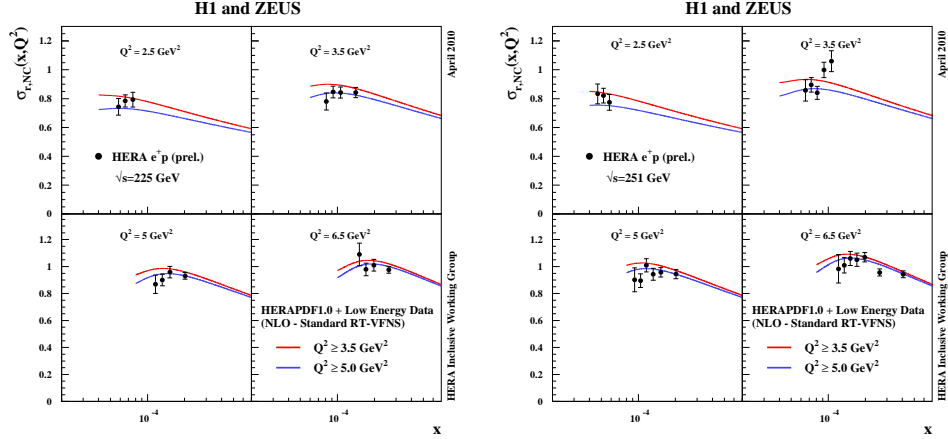


Fig. 30: The combined HERA data from running with proton beam energies $E_p = 460$ GeV and $E_p = 575$ GeV is shown for a few low- Q^2 bins, compared to predictions from PDF fits to these data and the combined HERA-I high energy data. Predictions are shown for data subject to two different minimum Q^2 cuts: 3.5 GeV^2 and 5.0 GeV^2 .

4.1.3 Including Low Energy run data in PDF fits

The preliminary combined data from the low energy running described in Sec 3.3 have been input to the HERAPDF fit together with the HERA-I combined high energy data. These data have 25 sources of correlated systematic uncertainty from the individual experiments, and 3 procedural sources of systematic uncertainty similarly to the high energy combination. These correlated errors are added in quadrature except for the 3 procedural which are treated as fully correlated by the Hessian method. There are 224 combined data points on the NC e^+p cross section from the low energy proton beam running and when they are fit together with the 592 combined data points from the HERA-I running the χ^2/ndf is 845.7/806 for 10 parameters. The partial χ^2/ndp are 588/592 for the high energy inclusive data and 257.6/224 for the low energy inclusive data. These data are sensitive to the minimum Q^2 cut imposed, as illustrated in Fig. 30. A better fit is obtained with a larger, $Q^2 > 5 \text{ GeV}^2$, cut. The partial χ^2/ndp after this cut are 527.1/566 and 200/215 for the low energy data. The data at low x , Q^2 access high y and thus sensitive to the longitudinal structure function F_L . Because of the close relationship of F_L and the gluon PDF these data should affect the gluon PDF. This is illustrated in Fig. 31 which shows that variation of the Q^2 -cut affects the gluon PDF more for the fit including low energy data, since the result is outside the error bands which include this cut-variation for the HERAPDF1.0 fit. Kinematically cutting out low Q^2 data also implies cutting out data at the lowest x and the data are similarly sensitive to an $x > 0.0005$ cut. Data at low x may not be well fit by the DGLAP formalism since this is missing $\ln(1/x)$ resummation terms and possible non-linear effects. Fig 31 also illustrates sensitivity to a 'saturation' inspired cut of $Q^2 > 1.0x^{-0.3} \text{ GeV}^2$. However, one cannot claim that any break-down of the DGLAP formalism has yet been observed, since if the HERAPDF1.0 formalism is generalised to the extended parametrisation with 14 parameters, then the increased uncertainty in the low- x gluon, illustrated in Fig. 34, covers the sensitivity of the low energy data to the low x , Q^2 cuts.

4.1.4 HERAPDF1.5

The HERAPDF1.5 NLO fit uses the same formalism as HERAPDF1.0 but includes preliminary HERA-I+II data. The χ^2 per degree of freedom for the HERAPDF1.5 NLO central fit is 760/664, where the increased χ^2 reflects the greater accuracy of the HERA-I+II combination. This fit has already been compared to the data in Figs. 8- 10. The improvement to the PDFs is illustrated in Fig. 32, which shows the HERAPDF1.5 in a format such that it may be directly compared with HERAPDF1.0 in Fig. 22. Fig. 33 shows the HERAPDF1.5 overlayed on HERAPDF1.0 on a linear x scale, such that the improvement at high x may be clearly seen.

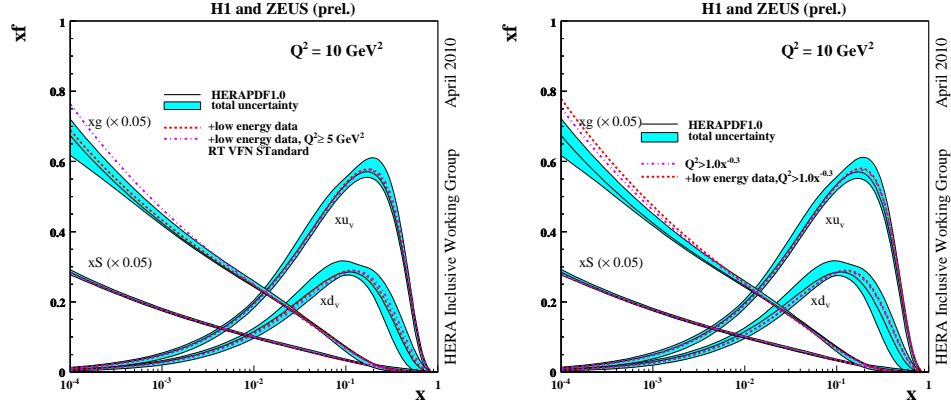


Fig. 31: The parton distribution functions from HERAPDF1.0, xu_v , xd_v , $xS = 2x(\bar{U} + \bar{D})$, xg , at $Q^2 = 10 \text{ GeV}^2$. The total uncertainties are shown. The gluon and sea distributions are scaled down by a factor 20. (Left) The lines overlayed show the results of fits to the HERA-1 data plus the low energy running data with the standard minimum Q^2 cut of 3.5 GeV^2 and with a harder cut of 5.0 GeV^2 . (Right) The lines overlayed show the results of fits to the HERA-1 data and to the HERA-1 plus the low energy running data, with the 'saturation inspired' cut of $Q^2 > 1.0x^{-0.3} \text{ GeV}^2$.

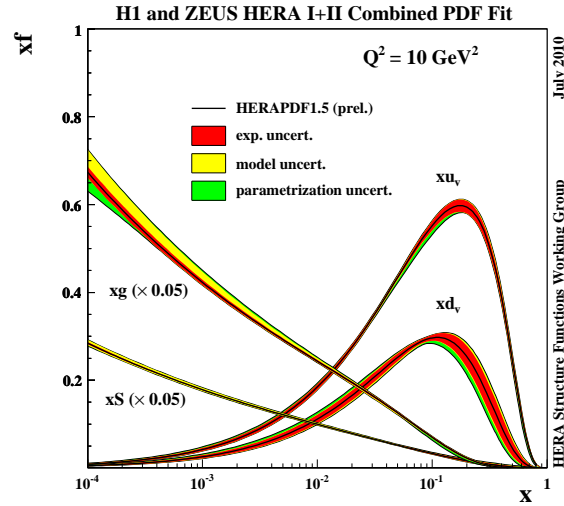


Fig. 32: The parton distribution functions from HERAPDF1.5, xu_v , xd_v , $xS = 2x(\bar{U} + \bar{D})$, xg , at $Q^2 = 10 \text{ GeV}^2$. The experimental, model and parametrisation uncertainties are shown separately. The gluon and sea distributions are scaled down by a factor 20.

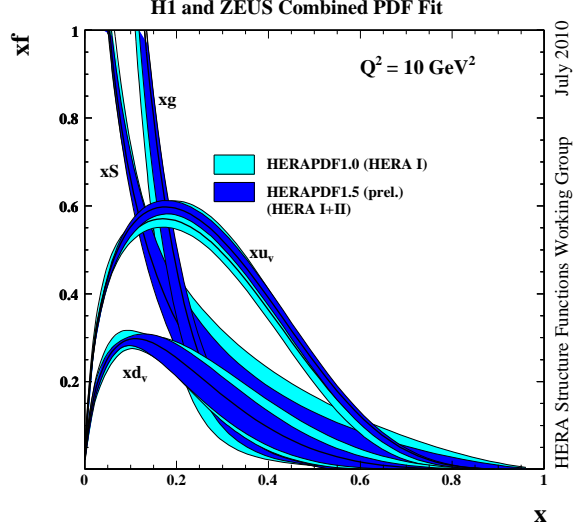


Fig. 33: The parton distribution functions from HERAPDF1.5, xu_v , xd_v , $xS = 2x(\bar{U} + \bar{D})$, xg , at $Q^2 = 10 \text{ GeV}^2$, overlayed on the parton distributions from HERAPDF1.0. The total uncertainties for each PDF are shown. A linear scale in x is used to emphasize the reduction in uncertainties for HERAPDF1.5 at high x .

The fit formalism was also extended to include more PDF parameters, as already described in Sec. 4. This fit, called HERAPDF1.5f NLO fit, has χ^2 per degree of freedom 730/664, where the improvement to the χ^2 is mostly due to the treatment of the three procedural systematic errors by the Hessian rather than Offset method. There is a small decrease in χ^2 , $\Delta\chi^2 = -5$ due to the increase of the number of parameters from 10 to 14. The PDFs of the HERAPDF1.5f and 1.5 NLO fits are compared in Fig. 34, where one can see that the extra freedom in the parametrisation does not change the central values of the PDFs significantly. The total size of the PDF uncertainties are also not changed significantly, although some of the parametrisation uncertainty in HERAPDF1.5 is now included in the experimental uncertainty in HERAPDF1.5f. The most significant change to the uncertainties is a modest increase in the uncertainty of the low- x gluon. This covers the sensitivity to low- x , Q^2 cuts found in the low energy data combination, see Sec. 4.1.3.

The HERAPDF1.5 NNLO fit was performed on the same preliminary combined HERA I+II data. The χ^2 per degree of freedom for the HERAPDF1.5 NNLO central fit is 740/664. For this NNLO fit the addition of extra parameters made a significant difference to the χ^2 . The change from a 10 to 14 parameter fit, results in a change of $\Delta\chi^2 = -32$ with the largest difference coming from the addition of the term which allows freedom in the low x gluon. Fig. 35 compares the HERAPDF1.5 NNLO fit to HERAPDF1.0 NNLO which was an NNLO version of the HERAPDF1.0 using just 10 parameters and fitting just HERA-I data. One can see that the extra parameters give somewhat different shapes to the valence quarks and a much harder high- x gluon PDF.

Fig. 36 compares the HERAPDF1.5 NNLO fit to the corresponding NLO fit HERAPDF1.5f. These fits have the same number of parameters. The change from NLO to NNLO gives a somewhat steeper sea and softer gluon at low x consistent with the different rates of evolution at NNLO. The most striking difference is the greater level of uncertainty at low x for the NNLO fit. This is mostly due to sensitivity to the low Q^2 cut on the data. One might have expected that an NNLO fit would fit low x , Q^2 data better than an NLO fit, however this would seem not to be the case, see also ref. [73].

4.1.5 Including jet data in PDF fits: HERAPDF1.6

The gluon PDF contributes only indirectly to the inclusive DIS cross sections. However, the QCD processes that give rise to scaling violations in the inclusive cross sections, namely the QCD-Compton

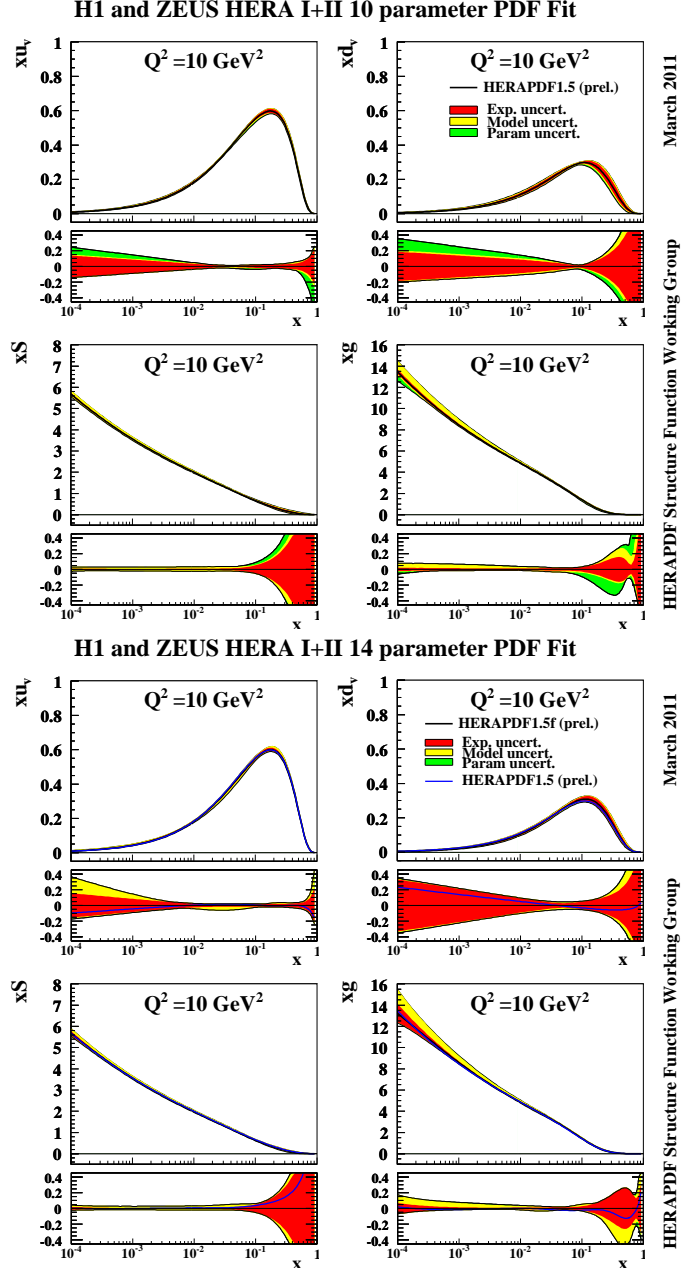


Fig. 34: The parton distribution functions from HERAPDF1.5 and HERAPDF1.5f, $xu_v, xd_v, xS = 2x(\bar{U} + \bar{D}), xg$, at $Q^2 = 10 \text{ GeV}^2$. Fractional uncertainty bands are shown below each PDF. The experimental, model and parametrisation uncertainties are shown separately.

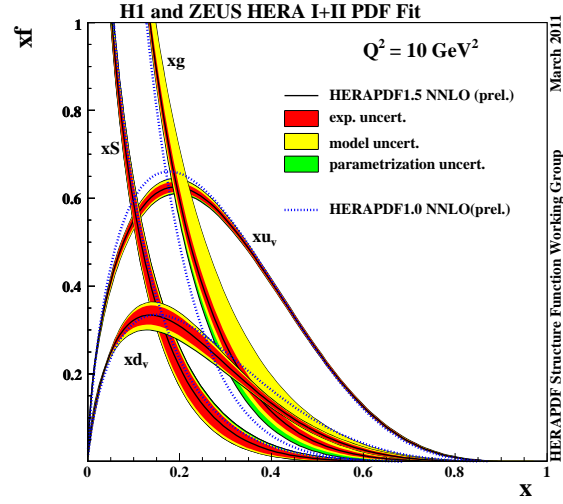


Fig. 35: The parton distribution functions from HERAPDF1.5 NNLO, $xu_v, xd_v, xS = 2x(\bar{U} + \bar{D}), xg$, at $Q^2 = 10 \text{ GeV}^2$, compared to HERAPDF1.0 NNLO. A linear scale in x is used to emphasize the differences at high x .

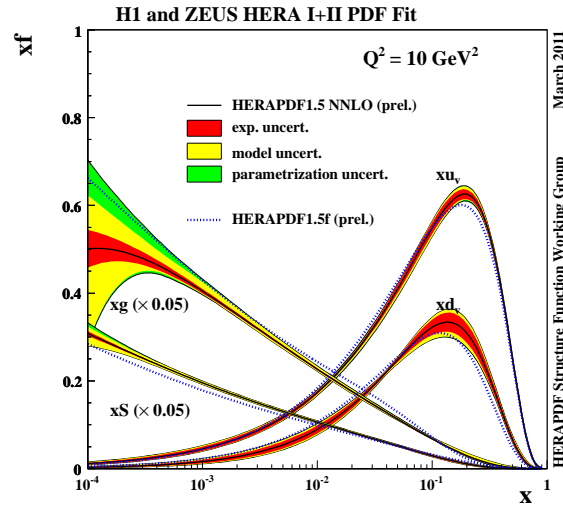


Fig. 36: The parton distribution functions from HERAPDF1.5 NNLO, $xu_v, xd_v, xS = 2x(\bar{U} + \bar{D}), xg$, at $Q^2 = 10 \text{ GeV}^2$, compared to the HERAPDF1.5f NLO fit. The gluon and sea distributions are scaled down by a factor 20.

(QCDC) and boson-gluon-fusion (BGF) processes, can also be observed as events with distinct jets in the final state provided that the energy and momentum transfer are large enough. The cross section for QCDC scattering depends on $\alpha_s(M_Z)$ and the quark PDFs. The cross section for the BGF process depends on $\alpha_s(M_Z)$ and the gluon PDF. These two processes are dominant in different kinematic regions. Thus jet cross sections give new information about the PDFs. For the inclusive data, the correlation between $\alpha_s(M_Z)$ and the gluon PDF limits the accuracy with which either can be determined. The jet data bring new information which helps to reduce the overall correlation.

In the HERAPDF1.6 NLO PDF fit the jet data sets presented in Sec. 3.5 are fitted together with the preliminary HERA I+II combined inclusive data. These data sets have 12 correlated systematic errors, which are treated as fully correlated by the Hessian method. The predictions for the jet cross sections have been calculated to NLO in QCD using the NLOjet++ program [74] and have been input to the fit by the FASTNLO interface [75]. The calculation of the NLO jet cross sections is too slow to be used iteratively in a fit. Thus NLOjet++ is used to compute LO and NLO weights which are independent of α_s and the PDFs. The FASTNLO program then calculates the NLO QCD cross sections, by convoluting these weights with the PDFs and α_s . The predictions must be multiplied by hadronisation corrections before they can be used to fit the data. These were determined by using Monte Carlo (MC) programmes, which model parton hadronisation to estimate the ratio of the hadron- to parton-level cross sections for each bin. The hadronisation corrections are generally within a few percent of unity. The predictions for jet production were also corrected for Z^0 contributions.

The fit is done with the same settings as for the HERAPDF1.5f fit. The χ^2/ndf for the fit is 812/766, for a fit to 674 inclusive data points and 106 jet data points with 14 parameters. The partial χ^2 of the data sets is 730/674 for the inclusive data and 82/106 for the jet data. Fig. 37 shows the parton distributions and their uncertainties for the HERAPDF1.6 fit. HERAPDF1.5f is also shown on this plot as a blue line. The fit with jets has rather similar central PDFs values to the fit without jets, apart from having a somewhat less hard high- x sea. The uncertainties are also similar to those of HERAPDF1.5f, with a slightly reduced uncertainty on the high- x gluon. The quality of the fit to the jet data establishes that NLO QCD is able simultaneously to describe both inclusive cross sections and jet cross sections, thereby providing a compelling demonstration of QCD factorisation.

The standard value of $\alpha_s(M_Z)$ used in the fits has been $\alpha_s(M_Z) = 0.1176$. The correlation between $\alpha_s(M_Z)$ and the gluon PDF is too strong to make an accurate determination of $\alpha_s(M_Z)$ using purely inclusive data, but the jet data are sensitive to $\alpha_s(M_Z)$ such that one may let it be a free parameter of the fit. The value of $\alpha_s(M_Z)$ which results is $\alpha_s(M_Z) = 0.1202 \pm 0.0013(\text{exp}) \pm 0.0007(\text{model/param}) \pm 0.0012(\text{had}) + 0.0045/-0.0036(\text{scale})$. We estimate the model and parametrisation uncertainties for $\alpha_s(M_Z)$ in the same way as for the PDFs and we also add the uncertainties in the hadronisation corrections applied to the jets. The scale uncertainties are estimated by varying the renormalisation and factorisation scales chosen in the jet publications by a factor of two up and down. The dominant contribution to the uncertainty comes from the jet renormalisation scale variation. Fig. 4.1.5 shows a χ^2 scan vs $\alpha_s(M_Z)$ for the fits with and without jets, illustrating how much better $\alpha_s(M_Z)$ is determined when jet data are included. The model and parametrisation errors are also much better controlled.

The χ^2 for the HERAPDF1.6 fit with free $\alpha_s(M_Z)$ is 807.6 for 765 degrees of freedom. The partial- χ^2 for the inclusive data has barely changed but the partial- χ^2 for the jet data decreases to 77.6 for 106 data points. Fig. 39 shows the summary plots of the PDFs for HERAPDF1.5f and HERAPDF1.6, each with $\alpha_s(M_Z)$ left free in the fit. It can be seen that without jet data the uncertainty on the gluon PDF at low x is large due to the strong correlation between the low- x shape of the gluon PDF and $\alpha_s(M_Z)$. However once jet data are included the extra information on gluon induced processes reduces this correlation and the resulting uncertainty on the gluon PDF is not much larger than it is for fits with $\alpha_s(M_Z)$ fixed.

Direct photoproduction dijet cross sections have also been used in PDF fits to constrain the gluon as for example in the ZEUS-jets analysis of ZEUS inclusive cross-section data and jet data [76] However,

H1 and ZEUS HERA I+II PDF Fit with Jets

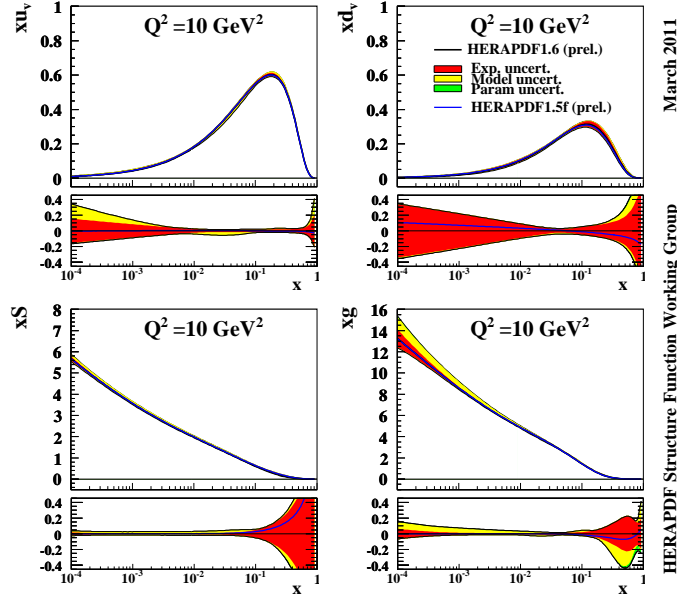


Fig. 37: The parton distribution functions from HERAPDF1.6, xu_v , xd_v , $xS = 2x(\bar{U} + \bar{D})$, xg , at $Q^2 = 10 \text{ GeV}^2$. Fractional uncertainty bands are shown below each PDF. The experimental, model and parametrisation uncertainties are shown separately. the central fit of HERAPDF1.5f is shown as a blue line

such data have not yet been used in the HERAPDF fits because the cross-section predictions for photo-produced jets are sensitive to the choice of the input photon PDFs. In order to minimise sensitivity to this choice, the analysis can be restricted to use only the ‘direct’ photoproduction cross sections. These are defined by the cut $x_\gamma^{\text{obs}} > 0.75$, where x_γ^{obs} is a measure of the fraction of the photon’s momentum that enters into the hard scatter. This is a direction for further study

4.1.6 Bringing it all together: HERAPDF1.7

Finally an NLO fit has been made bringing together all the data sets: HERA I+II combined high energy data, combined low energy running data, $F_2^{c\bar{c}}$ data and jet data. This fit is called HERAPDF1.7 [54]. The charm data are fit in the optimized version of the RT heavy quark scheme, with its preferred value of $m_c = 1.5$. The value of $\alpha_s(M_Z) = 0.119$ is fixed. This value gives the best fit to all the data in

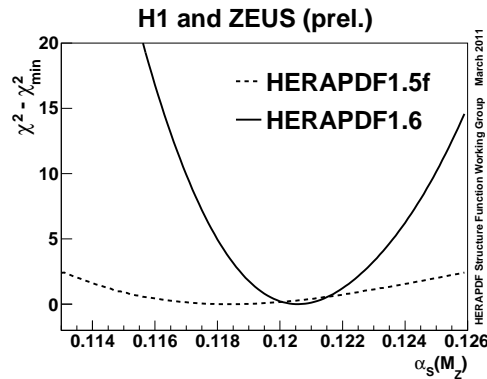


Fig. 38: The difference between χ^2 and its minimum value for the HERAPDF1.5f and HERAPDF1.6 fits as a function of $\alpha_s(M_Z)$

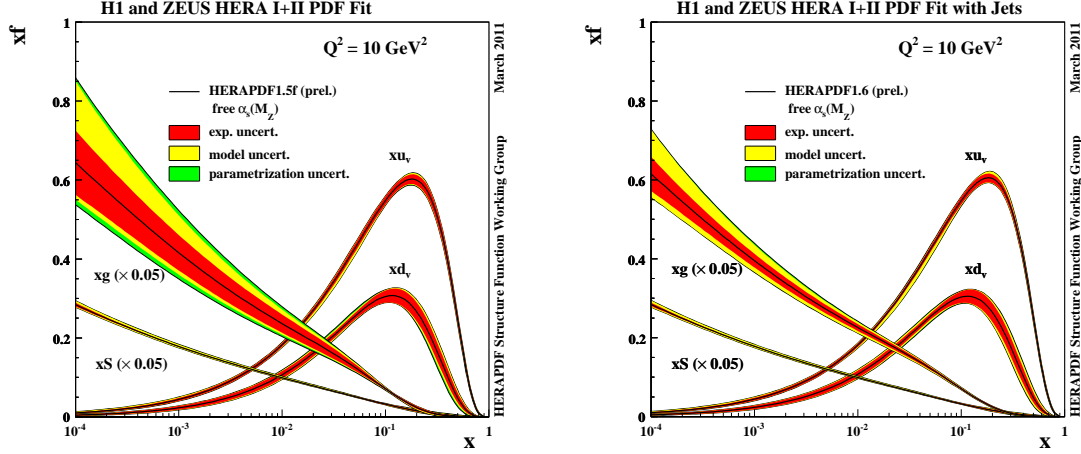


Fig. 39: The parton distribution functions $xu_v, xd_v, xS = 2x(\bar{U} + \bar{D}), xg$, at $Q^2 = 10 \text{ GeV}^2$, from HERAPDF1.5f and HERAPDF1.6, both with $\alpha_S(M_Z)$ treated as a free parameter of the fit. The experimental, model and parametrisation uncertainties are shown separately. The gluon and sea distributions are scaled down by a factor 20.

this fit, with the jet data dominating the sensitivity. Other settings are as for the HERAPDF1.6 fit except that the parameter D_{uv} was found to be consistent with zero and hence only 13 parameters have been used for the HERAPDF1.7 fit. The correlated systematic uncertainties of the data sets are treated as for the individual fits: for the inclusive combined data sets at both low and high energy only the procedural errors are treated as correlated by the Hessian method. For the F_2^{cc} data one source is treated as correlated by the offset method and for the jet data all 12 sources are treated as correlated by the Hessian method.

The overall χ^2/ndf is 1097.6/1032 with partial χ^2/ndp of: 44.1/41 for F_2^{cc} data; 226.6/224 for low energy data; 80.6/106 for jet data and 746/674 for HERA-I+II high energy data. The data are all very compatible. The results of this combined fit are illustrated in Fig. 40

4.2 Comparison of HERAPDF to other PDFs

Fig. 41 compares HERAPDF1.5 to MSTW08 [65], CTEQ6.6 [77], CT10 [78], NNPDF2.1 [80], ABKM09 [81], JR09 [82] at $Q^2 = 10 \text{ GeV}^2$. All PDFs are shown with 68% CL uncertainties. The top row compares NLO PDFs and the bottom row compares NNLO PDFs. These PDF sets have been chosen for comparison because they have been selected for benchmarking by the PDF4LHC group [83] (though CT10 and NNPDF2.1 are updates of the benchmarked PDFs). All PDFs are broadly compatible but there are differences of detail which can have important consequences for predictions of LHC cross sections.

A concise way to compare predictions for various LHC cross sections is to compare parton-parton luminosities for quark-antiquark and gluon-gluon interactions.

$$\frac{\partial L_{gg}}{\partial \hat{s}} = \frac{1}{s} \int_{\tau}^1 \frac{dx_1}{x_1} f_g(x_1, \hat{s}) f_g(x_2, \hat{s}) \quad (16)$$

$$\frac{\partial L_{\Sigma(\bar{q}q)}}{\partial \hat{s}} = \frac{1}{s} \int_{\tau}^1 \frac{dx_1}{x_1} \sum_{q=d,u,s,c,b} [f_q(x_1, \hat{s}) f_{\bar{q}}(x_2, \hat{s}) + f_{\bar{q}}(x_1, \hat{s}) f_q(x_2, \hat{s})] \quad (17)$$

where s is the centre of mass energy squared of the proton-proton collision and x_1 and x_2 are the fractional momenta of the partons in each proton, such that the centre of mass energy squared of the parton-parton collision is, $\hat{s} = \tau s$, where $\tau = x_1 x_2$.

Fig. 42 shows $q - \bar{q}$ and $g - g$ luminosities for $p - p$ interactions at the LHC² with $\sqrt{s} = 7 \text{ TeV}$, in ratio to those of the MSTW2008 PDF, for PDFs issued by CTEQ, NNPDF and HERAPDF. This figure

²Plots on top and middle rows from G.Watt <http://projects.hepforge.org/mstwpdf/pdf4lhc>

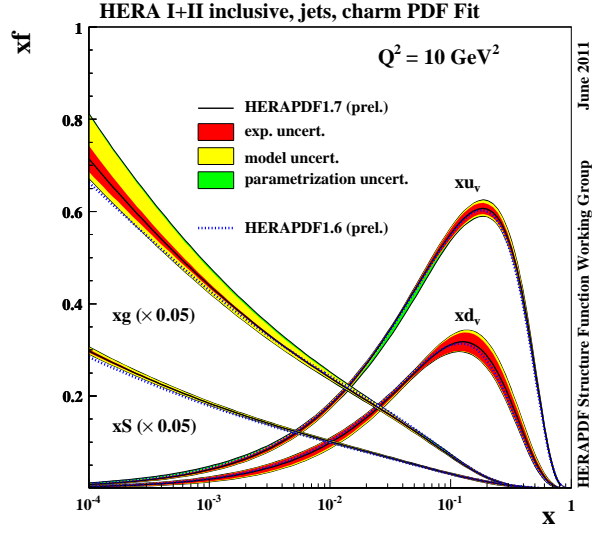


Fig. 40: The parton distribution functions from HERAPDF1.7, $xu_v, xd_v, xS = 2x(\bar{U} + \bar{D}), xg$, at $Q^2 = 10 \text{ GeV}^2$. The experimental, model and parametrisation uncertainties are shown separately. The sea and gluon distributions are scaled down by a factor 20.

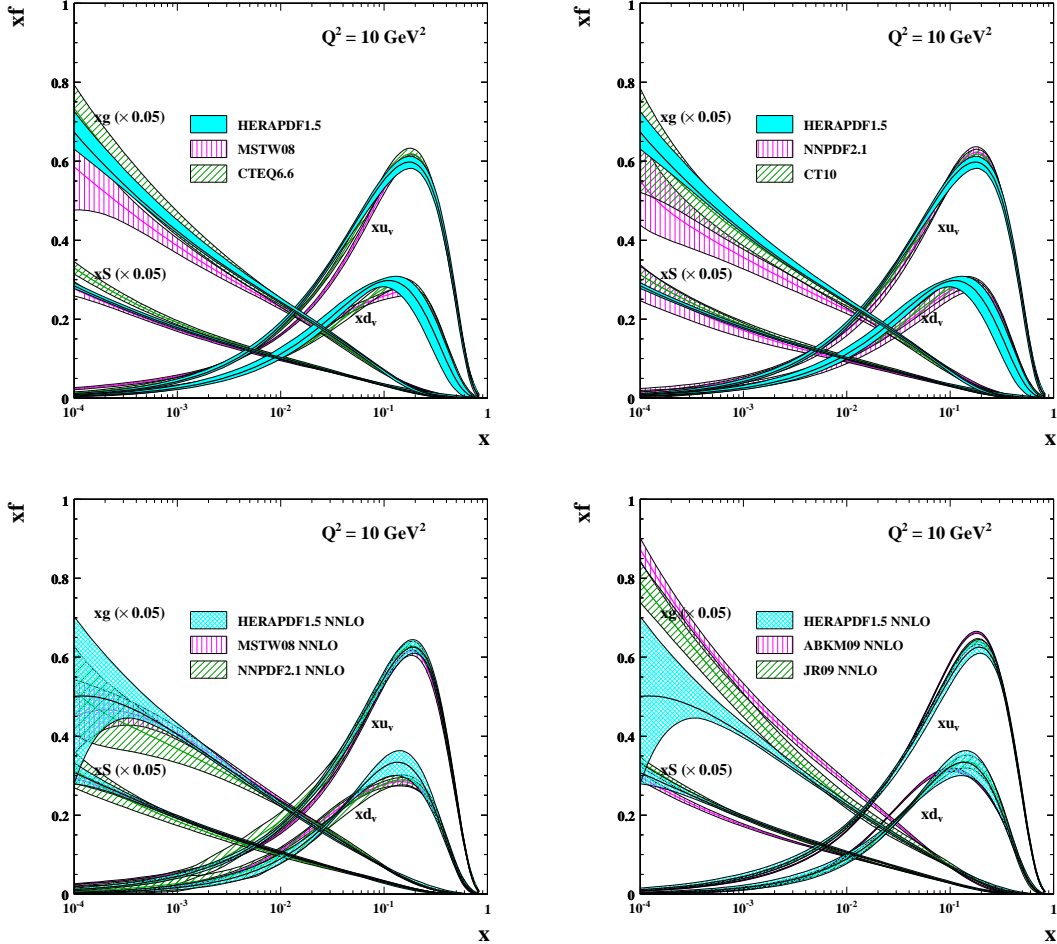


Fig. 41: HERAPDF1.5 compared to other PDFs. Top: NLO PDFs from MSTW08, CTEQ66, NNPDF2.1, CT10. Bottom: NNLO PDFs from MSTW08, NNPDF2.1, ABKM09, JR09

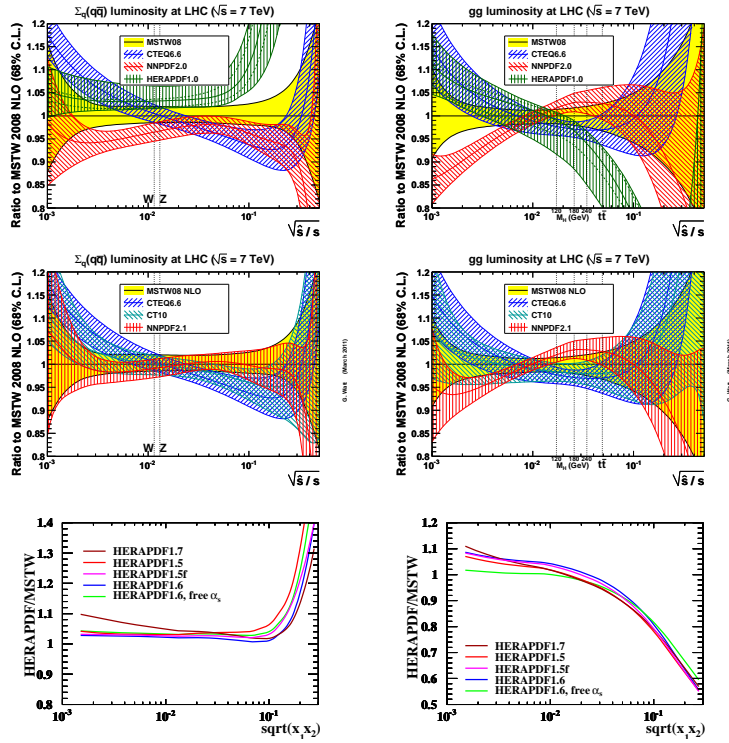


Fig. 42: Left hand side: the $q - \bar{q}$ luminosity in ratio to that of MSTW2008 for various PDFs. Right hand side: the same for the $g - g$ luminosities. Upper row, PDFs as benchmarked by the PDF4LHC group: middle row, updates for CT10 and NNPDF2.1 issued in 2011: bottom row, the HERAPDF NLO updates described in this review.

also shows the corresponding luminosity plots for the HERAPDF1.5, 1.6, 1.7 NLO updates described in this review. Fig. 43 shows similar luminosity comparison plots for NNLO PDFs from MSTW, ABKM, JR and HERAPDF.

There are several reasons why the PDF predictions differ. It is beyond the scope of the current review to describe all the other PDFs in detail. However a few remarks can be made on the main differences between HERAPDF and other PDFs. Firstly they are based on different data sets and different choices of cuts on these data sets and this is closely related to the differing way in which the PDF uncertainties are estimated since the use of many different data sets has led to the use of increased χ^2 tolerances for some of the PDF sets. Secondly, different choices of PDF parametrisation are made and this impacts on the size of the uncertainties. Thirdly, PDFs use different central values of $\alpha_s(M_Z)$ and this affects the shape of the PDFs, particularly the gluon PDF. Fourthly, the PDF analyses differ in the schemes used to account for heavy quark production and different heavy quark masses.

4.2.1 Correlated systematic uncertainties and χ^2 tolerance.

Most modern data used in PDF fits are statistically very precise such that systematic errors dominate. Thus the correct treatment of correlated systematic errors becomes very important. In PDF fits done prior to the year 2000 point-to-point correlated systematic errors were not specifically treated. They were added in quadrature to the uncorrelated errors. This can lead to biased results. The correct treatment of correlated systematic errors is discussed in Ref [68]. The consensus amongst PDF fitters is that the uncertainty due to correlated systematic errors should be included in the theoretical prediction such that

$$F_i(p, s) = F_i^{\text{NLOQCD}}(p) + \sum_{\lambda} s_{\lambda} \Delta_{i\lambda}^{\text{sys}}$$

where p are the PDF parameters, s_{λ} represent independent (nuisance) variables for each source of systematic uncertainty and $\Delta_{i\lambda}^{\text{sys}}$ represents the one standard deviation correlated systematic error on data

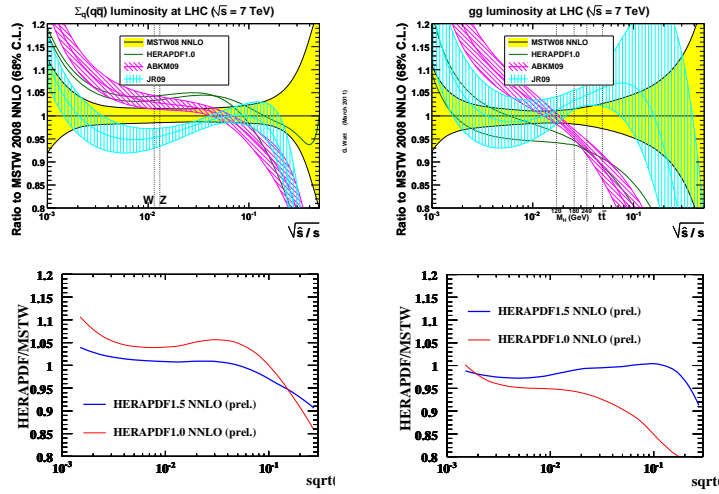


Fig. 43: Left hand side: the $q - \bar{q}$ luminosity in ratio to that of MSTW2008 for various PDFs. Right hand side: the same for the $g - g$ luminosities. Upper row, NNLO PDFs as benchmarked by the PDF4LHC group (*Plots from G.Watt <http://projects.hepforge.org/mstwpdf/pdf4lhc/>*): bottom row, the HERAPDF1.5 NNLO PDFs described in this review compared to HERAPDF1.0 NNLO

point i due to correlated error source λ . A representative form of the χ^2 is then given by

$$\chi^2 = \sum_i \frac{[F_i(p, s) - F_i(\text{meas})]^2}{\sigma_i^2} + \sum_\lambda s_\lambda^2 \quad (18)$$

where σ_i is the uncorrelated error on each data point. Thus the nuisance parameters are fitted together with the PDF parameters. This method of treatment of correlated systematic has been termed the Hessian method. An alternative is the Offset method in which $s_\lambda = 0$ for the central fit but the nuisance parameters are varied when determining the error on the PDF parameters [68].

In the PDF fits of CTEQ/CT, MSTW and GJR/JR the Hessian method is used with increased χ^2 tolerances such that a 68%(90%)CL is not set by a variation of $\Delta\chi^2 = 1(2.73)$ but by a larger variation. The reason for the use of such increased χ^2 tolerances arises when using many different input data sets which are not all completely consistent. The tolerances are set so as to ensure that all the separate data sets are fit to within their 68%(90%)CL. The tolerance can differ according to the parameter being fitted (or more exactly according to an eigenvector combination of parameters, see Sec. 4.2.2) but as a rough guide the CTEQ 90%CL tolerance is $\Delta\chi^2 \sim 100$ and the MSTW 90%CL tolerance is $\Delta\chi^2 \sim 30$ for the MSTW2008 analysis³. The GJR/JR analyses use $\Delta\chi^2 \sim 50$. The use of these increased χ^2 tolerances has caused great controversy. For example, Pumplin [84] argues that a χ^2 tolerance of at most ~ 10 can be justified on the grounds of data incompatibility and that the more inflated values implicitly account for parametrisation variations.

The ABKM group does not use increased tolerances and that is why their PDF uncertainties are generally smaller than those of other groups. HERAPDF also does not use an increased tolerance but considers additional model and parametrisation uncertainties, see Sec. 4. The NNPDF group use a completely different method of estimating PDF uncertainties, see Sec 4.2.4.

For the HERAPDF the Hessian procedure has already been applied to the data combination to set the best values for the systematic shifts and the combination procedure itself results in greatly reduced systematic errors, such that there is no longer a significant difference in the PDF uncertainties obtained using the Offset and Hessian methods of treating systematic uncertainties. The good χ^2 for the combination fit also establishes that the resulting data set is very consistent, see Sec. 3.1, such that in the HERAPDF the conventional tolerance $\Delta\chi^2 = 1$ is appropriate for setting 68%CL uncertainties.

³Note that MSTW provide both 68% CL and 90%CL uncertainties, whereas for CTEQ/CT a factor of $1./\sqrt{2.73}$ must be applied to the 90%CL uncertainties to obtain 68%CL uncertainties.

4.2.2 Diagonalisation and Eigenvector PDF sets

In either the Hessian or the Offset method, the Hessian matrices and covariance matrices are not, in general, diagonal. The variation of χ^2 w.r.t. some parameters is much more rapid than that of others, but because the parameters are correlated to each other the effect of each parameter is not clear. When evaluating uncertainties on physical observables it can be an advantage to use an eigenvector basis of PDFs, which provide an optimized representation of parameter space in the neighbourhood of the minimum. The eigenvalues of the covariance matrix represent the squares of the errors on the combination of parameters which gives the corresponding eigenvector.

An eigenvector basis of PDFs is the usual way of summarizing the results of a PDF analysis including its error estimates. Two sets of PDF parameters must be supplied for each eigenvalue, representing displacement up and down along its eigenvector direction by the χ^2 tolerance. The symmetric error on a quantity F which is a function of the PDF parameters is then simply given by

$$< \sigma_F^2 > = \sum_j \left[\frac{F(p_j^+) - F(p_j^-)}{2} \right]^2$$

where $F(p_j^+)$, $F(p_j^-)$ are the values of F evaluated up and down along eigenvector j . Asymmetric errors may be evaluated by the prescription:

$$< \sigma_F^2(+) > = \sum_j \left[\max(F(p_j^+) - F(p_j^0), F(p_j^-) - F(p_j^0), 0) \right]^2$$

$$< \sigma_F^2(-) > = \sum_j \left[\max(F(p_j^0) - F(p_j^-), F(p_j^0) - F(p_j^+), 0) \right]^2$$

where $F(p_j^0)$, is the central value of F .

The PDFs from the HERAPDF are made public in this format via the LHAPDF (<http://lhapdf.hepforge.org>) interface. As well as the eigenvector sets, which give the experimental uncertainty of the HERAPDF, further sets are provided to cover the model and parametrisation variations. These should be combined with the experimental errors as specified in Sec. 4.1. Further PDF sets are also provided for a range of fixed $\alpha_s(M_Z)$ values, so that uncertainty due to $\alpha_s(M_Z)$ variation may also be evaluated.

The LHAPDF library is also the repository for the PDF sets from other PDF fitting groups.

4.2.3 Choice of data sets and kinematic cuts

The CTEQ6.6, MSTW2008, ABKM09 and JR09 PDF analyses do not use the recently combined inclusive cross section data from HERA-I [5] which are up to three times more accurate than the separate H1 and ZEUS data sets used by previous PDF analyses. These combined HERA data are shifted in normalisation by $\sim 3\%$ with respect to the previous HERA data, and this explains the higher luminosity of the HERAPDF at low τ .

Conversely the HERAPDF analysis uses only HERA data, whereas the CTEQ, MSTW and NNPDF analyses are 'global' PDFs which also use: older fixed target data, both from DIS and from Drell-Yan production; Tevatron W , Z cross section data and jet production data. The ABKM and JR PDFs each use some but not all of these non-HERA data sets.

The use of a single consistent data set with a clear statistical interpretation of uncertainty limits was one of the primary motivations behind the HERAPDF. However there are other reasons why the use of some of the other data sets may lead to further uncertainties. Firstly, the neutrino- Fe fixed-target scattering data from CCFR and NuTeV, which is often used to help to determine the valence densities, needs corrections for nuclear effects (the 'EMC effect'). Although such nuclear corrections are made in the global PDF analyses, they are not perfectly determined and the uncertainty due to these corrections is

not fully accounted [55]. More recently similar criticisms have been made of the use of deuterium target data (either in DIS or Drell-Yan). Accardi et al [56] have reconsidered deuterium corrections for the fixed target data. They find large uncertainties in these corrections and this results in greater (unaccounted for) uncertainty in the high- x d -quark for fits where the deuterium data is the principal source of information on the d -quark. (For the HERAPDF the information on d -quark comes from CC e^+p scattering).

Fixed proton target data do not suffer from these problems, but the kinematic reach of such data does extend into the high- x , low- Q^2 region, where the theoretical interpretation of the data requires consideration of target mass corrections and higher twist terms. Most PDF analyses make a $W^2 \gtrsim 15\text{GeV}^2$ cut to avoid this region (for the HERAPDF this is unnecessary since all HERA data is at large W). The ABKM analysis chooses to include the low W data and model the higher twist terms. The high- x region is also receiving attention from the CTEQ-JLAB group [85].

A further problem in the use of older fixed target data is that results were often presented and used in terms of F_2 rather than reduced cross sections. ABM [86] have examined the use of NMC F_2 data in the global fits. The NMC extraction of F_2 relied on assumptions on the value of F_L which are not consistent with modern QCD calculations. ABM find that using NMC published values of F_2 , rather than the NMC cross section data, raises their extracted values of α_S erroneously.

The HERAPDF avoids bias from erroneous assumptions about heavy target corrections, deuterium corrections, higher twist corrections and F_L corrections, by using only HERA pure proton target cross section data, but a price is paid in terms of the uncertainties of the high- x parton distributions, which are generally larger than those of the other groups.

It is also notable that the HERAPDFs have a harder high- x sea and a softer high- x gluon PDF at NLO. It has been suggested that this may be because Tevatron jet data are not included in the HERAPDF fit. However the story is not quite so simple.

Global fits use Tevatron high- E_T jet production data to help to pin down the high- x gluon. The HERAPDF analysis uses HERA-jet data for the same purpose, although the HERA jet data do not extend to as high x values as the Tevatron jet data. These Tevatron jet data have very large correlated systematic uncertainties compared to HERA jet data such that much trust must be put in the evaluation of systematic uncertainties. Tevatron Run-I jet data suggested a hard high- x gluon, but Run-II data soften this. The MSTW analysis uses only Run-II data whereas the CT/CTEQ analyses use both Run-I and Run-II data. These choices can explain the harder gluon luminosities of the CT PDFs at high- x . Watt and Thorne [87] obtain poor χ^2 when comparing the Tevatron jet data to the HERAPDF1.0, 1.5 predictions. However their fits only compare to the central predictions of the HERAPDF. A more valid comparison would account for the HERAPDF error bands. If the Tevatron jet data are input to the HERAPDF1.5 fit a much better χ^2 ($\chi^2/ndp = 1.48$ for CDF and 1.35 for D0 jets) is obtained. Significantly, the resulting PDFs do not lie outside the HERAPDF1.5 error bands (although they do imply a harder high- x gluon- on the upper edge of the error band). The reason that the HERAPDF can give a reasonable description of Tevatron jet data, while still having a relatively soft high- x gluon PDF, is that high- E_T jets result not only from the high- x gluon but also from high- x quarks and HERAPDF has a rather hard high- x quark PDF.

The ABKM analysis also chooses not to use Tevatron jet data, partly because new physics effects may be hidden in the data, biasing the PDFs. Consequently, ABKM has a soft high- x gluon luminosity. Nevertheless, ABM gives a good description of Tevatron jet data [88]. A further issue regarding the use of Tevatron jet data concerns their use together with deuterium fixed-target data. The greater uncertainty in the high- x d -quark, due to uncertain deuterium corrections, will feed into the high- x gluon PDF, since the $d - g$ process provides a substantial part of the Tevatron jet cross section. However this larger uncertainty is usually not accounted for [56].

4.2.4 Parametrisation and model uncertainty

HERAPDF central fits have a relatively small number of parameters ~ 14 . However, parametrisation uncertainty is estimated by making fits with additional parameters freed, or with a change of the choice of the starting scale, Q_0^2 , which is equivalent to a re-parametrisation. The comparison of HERAPDF1.5, which uses 10 free parameters and HERAPDF1.5f which uses 14 free parameters in Fig. 34, shows that this procedure for accounting for parametrisation uncertainty largely accounts for the uncertainty introduced when the extra parameters are freed in the central fit.

The HERAPDF results in a similar central value and uncertainty estimates to those of the global PDFs in many kinematic regions. In the case of the central values this is because the HERA data dominate the global input data. In the case of the uncertainty estimates it is partly due to the fact that the HERAPDF experimental uncertainties are augmented by estimates of the model and parametrisation variations, which are not accounted in the CT and MSTW analyses. This lends support to the idea that the increased χ^2 tolerances of MSTW and CT partly cover some of these additional model and parametrisation uncertainties.

The NNPDF global analysis uses a completely different approach both to PDF parametrisation and to the determination of PDF uncertainties. All errors (statistical, systematic and normalisation) as given by experimental collaborations are represented by Monte Carlo replica sets of artificial data. A neural net is used to learn the shape of these replicas rather than using a fixed parametrisation at the starting point. This can be regarded as equivalent to using a very large number of parameters. The PDFs are not determined by a χ^2 fit but by stopping the learning algorithm before overlearning occurs. The results are not presented in terms of eigenvectors of the fit but in terms of a set of replicas such that their mean gives the best estimate of the central PDF and the standard deviation from this mean gives the 68%CL uncertainty estimate. It is remarkable that this entirely different procedure gives broadly similar central values and uncertainty estimates as those of the MSTW and CTEQ global fits. To some extent this vindicates the standard procedure, in particular with regard to the use of increased χ^2 tolerances to set the 68%CL uncertainties.

4.2.5 The value of $\alpha_s(M_Z)$

Some groups (HERAPDF, CTEQ, NNPDF) adopt a fixed value of $\alpha_s(M_Z)$, inspired by the PDG value, and others (ABKM, GJR, MSTW) fit $\alpha_s(M_Z)$ simultaneously with the PDF parameters and use their best fit value. All groups bar GJR use values $\sim 0.118 - 0.120$ at NLO but there is a definite low(0.113)-high(0.117) split at NNLO. HERAPDF, CT(EQ), NNPDF and MSTW provide PDFs at different $\alpha_s(M_Z)$ values so that the effect of variation of $\alpha_s(M_Z)$ on cross section predictions can be evaluated.

MSTW obtain the highest value of $\alpha_s(M_Z)$, at both NLO and NNLO, and these high values have been attributed to the use of Tevatron jet data in their fits. However, ABM have tried inputting these jet data to their fit and have found that this has only a small effect on their extraction of a low value of $\alpha_s(M_Z)$ [88]. There is also a 'folk-lore' that DIS data prefer lower values of $\alpha_s(M_Z)$. However both MSTW [89] and NNPDF [90] have performed DIS only fits in which they find that only the BCDMS data prefer low $\alpha_s(M_Z)$ values. The HERA data actually prefer quite high values as shown in Sec. 4.1.5. The effect of this on the gluon-gluon luminosity may be seen in Fig. 42 by comparing the HERAPDF1.6 curve, with fixed $\alpha_s(M_Z) = 0.1176$, to that of the HERAPDF1.6 free $\alpha_s(M_Z)$ curve, which has $\alpha_s(M_Z) = 0.1202$. The larger $\alpha_s(M_Z)$ value leads to a smaller low- x gluon and a somewhat harder high- x gluon such that the gluon-gluon luminosity is then in better agreement with that of MSTW2008, which also use a large $\alpha_s(M_Z)$ value.

4.2.6 Heavy Quark Schemes

The ABKM and GJR groups use Fixed-Flavour-Number (FFN) treatments, HERAPDF, CTEQ and MSTW use various General-Mass-Variable-Flavour-Number (GMVFN) treatments and NNPDF2.0 [79]

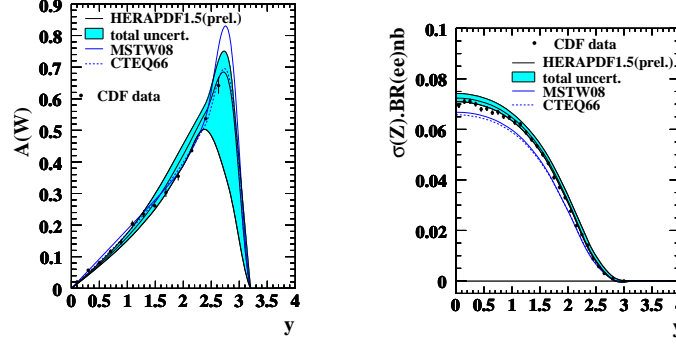


Fig. 44: Left hand side: data on the direct W -asymmetry from CDF; right hand side: data on the $Z0$ rapidity spectrum from CDF; compared to NLO predictions from CTEQ6.6, MSTW08 and HERAPDF1.5. The blue band indicates the uncertainties on the HERAPDF prediction.

used a Zero-Mass-Variable-Flavour-Number treatment (ZMVFN). These heavy quark schemes are discussed in Ref. [92]. The use of the zero-mass treatment explains why the NNPDF2.0 luminosities lie lower than those of CTEQ, MSTW and HERAPDF at low τ . This may be seen by comparing the top row of Fig. 42 to the middle row where the NNPDF2.1 luminosity, which used a GMVFN, is seen to be in much better agreement with the other PDFs. This is because, when charm mass is accounted for, charm is suppressed at threshold and the light quark densities must be somewhat larger in order to describe the deep inelastic cross-section. However not all GMVFNs are the same. Predictions for F_2^c differ between schemes [91] and the choice of scale within a scheme can also affect predictions. The value of the charm and beauty masses also differ between the PDF analyses. HERAPDF, NNPDF and MSTW now provide PDFs at different charm and beauty mass values so that the effect of this can be evaluated. In future the combined data on $F_2^{c\bar{c}}$, discussed in Sec. 4.1.2, should help to reduce the uncertainty on PDFs coming from the choice of scheme and the value of the charm mass.

The heavy quark mass schemes described in Sec. 4.1.2 all use a charm quark mass parameter which should be the pole-mass. However the pole-mass has a strong dependence on the order of the perturbative calculation and may best be regarded as a parameter. It may be better to consider the \overline{MS} running-mass. HERA data on $F_2^{c\bar{c}}$ has also been used for a determination of this mass [93]

4.3 Comparisons of HERAPDF predictions to Tevatron and LHC data

Finally we present some representative comparisons of HERAPDF predictions to PDF sensitive data from the Tevatron and LHC colliders. Fig. 44 presents comparisons to CDF data on the direct W -asymmetry [94] and $Z0$ rapidity spectrum [95]. These data are well described by the HERAPDF1.5 prediction⁴. A fit of the data to the central value of the prediction yields a χ^2 of 36 for 28 data points for the $Z0$ data and of 41 for 13 data points for the asymmetry data. These descriptions are improved if the data is input to the HERAPDF fit, to $\chi^2/ndp = 26/28$ for the $Z0$ data and 21/13 for the asymmetry data⁵. The resulting PDFs lie well within the HERAPDF1.5 error bands. The HERAPDF uncertainty bands could be reduced by input of these data. This is a future project beyond the scope of the current review.

Fig. 45 presents comparisons of HERAPDF1.0 predictions to D0 data on the inclusive jet production [96] Because of the large correlated systematics of these data it is not possible to assess the quality of the description by eye. If these data are input to the HERAPDF1.5 fit a $\chi^2/ndp = 145/110$ can be obtained. Similarly if CDF inclusive jet production data [97] are input to the HERAPDF1.5 NLO fit a $\chi^2/ndp = 113/76$ is obtained. In both cases the resulting PDFs move to the edge of the

⁴The predictions of the HERAPDF1.6 and 1.7 PDFs are very similar to that of HERAPDF1.5

⁵Note that the χ^2/ndp for these asymmetry data are as well described by the HERAPDF as they are by other PDFs which have used them, e.g. NNPDF.

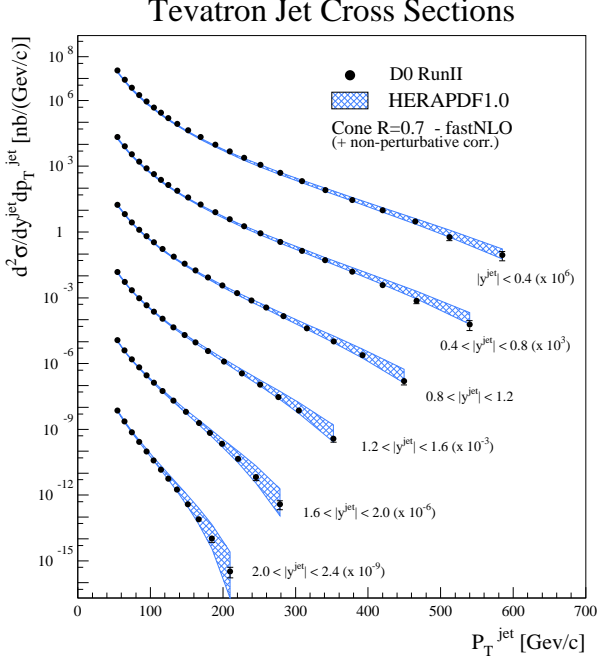


Fig. 45: D0 data on inclusive jet production compared to NLO predictions from HERAPDF1.0

HERAPDF1.5 error band- tending to favour a harder high- x gluon. For this reason, the HERAPDF1.6 $\alpha_s(M_Z) = 0.1202$ fit, which already has a harder gluon than the 1.5 fit, gives the best description of these data out of all the NLO HERAPDF sets.

The HERAPDF1.5NNLO PDF fit gives a better description of these data than the NLO PDFs- the central PDF of HERAPDF1.5NNLO yields a χ^2 per data point of $\chi^2/ndp = 72/76$. However this can only be approximate since the theoretical description of the jet data itself contains only an approximate calculation for the NNLO jet cross-section.

Fig. 46 presents comparisons of various PDFs, including HERAPDF1.5, to ATLAS data on the W -lepton decay pseudorapidity distributions and the Z^0 rapidity distribution, as well as on the W -lepton asymmetry [98]. Fig. 47 presents comparisons of HERAPDF1.5 predictions to 234pb^{-1} of preliminary CMS 2011 data on the W decay lepton asymmetry [100]. These LHC W and Z cross section data are well described by the HERAPDF. However, a detailed study by the ATLAS Collaboration [99] using the ATLAS W and Z data and the HERA-I combined data has indicated a preference of the ATLAS data for unsuppressed strangeness at $x \sim 0.01$. Further discussion of this is beyond the scope of the present review.

Fig. 48 presents comparisons of various PDF predictions, including HERAPDF1.5, to ATLAS data on the inclusive jet production [101]. Fig. 49 presents comparisons of various PDF predictions, including HERAPDF1.5, to CMS data on the inclusive jet production [102]. Because of the large correlated systematics of these data it is not possible to assess the quality of the description by eye. The ATLAS jet data are published with information on these correlations and a χ^2 per data point of $\sim 60/90$ can be obtained for each of the HERAPDFs, and the χ^2 for the MSTW, CT and NNPDFs are similar. Thus the data are not yet very discriminating, however they indicate a preference for a somewhat less hard high- x gluon than the Tevatron jet data.

5 Summary

Deep inelastic lepton-hadron scattering data from the HERA collider now dominate the world data on deep inelastic scattering since they cover an unprecedented kinematic range. The H1 and ZEUS experi-

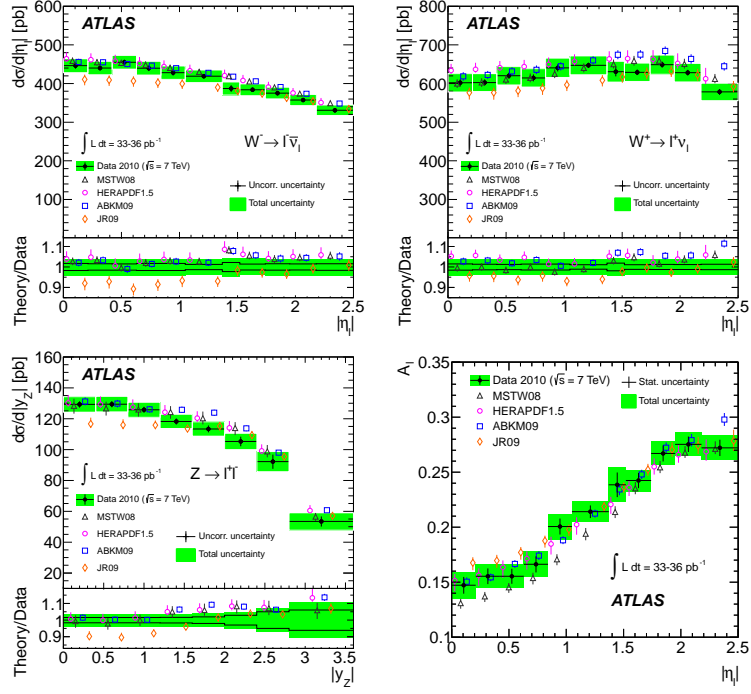


Fig. 46: Comparisons of ATLAS data on W^+ and W^- decay lepton pseudorapidity spectra, Z^0 rapidity spectra and W decay lepton asymmetry data to NNLO predictions from MSTW08, HERAPDF1.5, ABKM09, JR09.

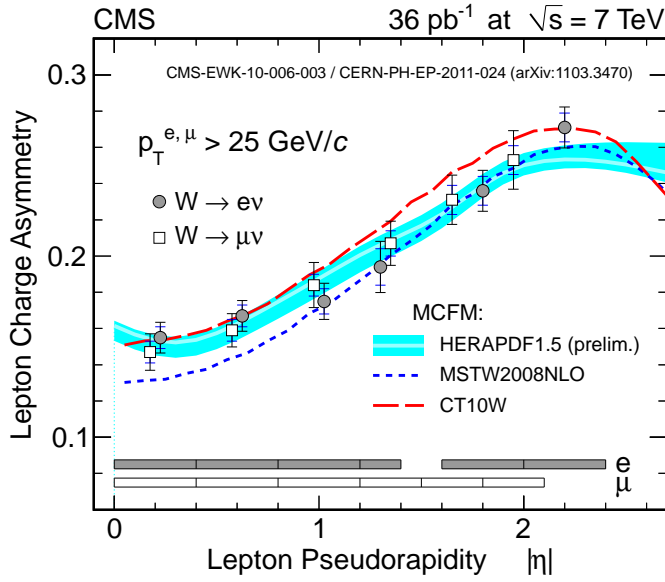


Fig. 47: CMS data on W decay lepton asymmetry compared to NLO predictions from HERAPDF1.5, MSTW08 and CT10W

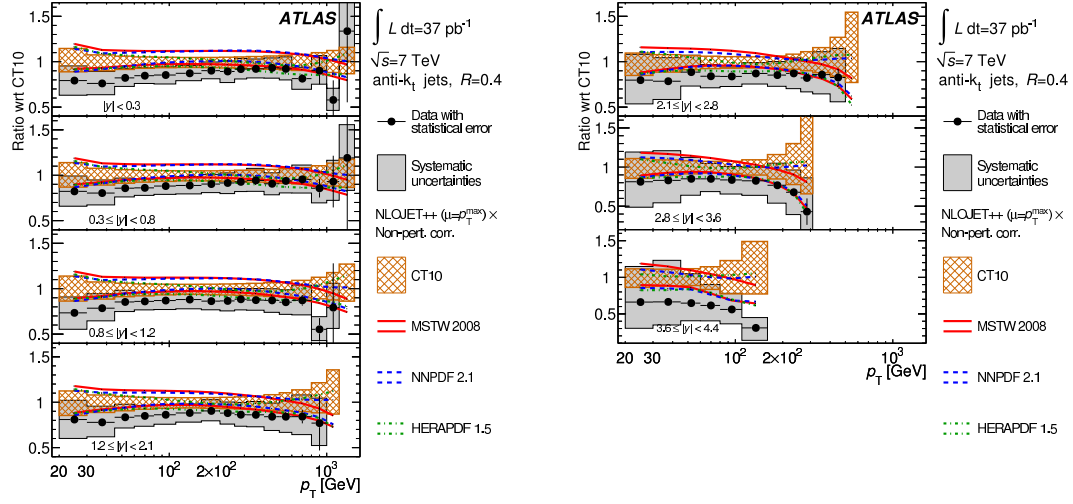


Fig. 48: ATLAS data on inclusive jet production in central and forward rapidity regions in ratio to the NLO predictions of CT10 and compared to NLO predictions from HERAPDF1.5, NNPDF2.1 and MSTW08

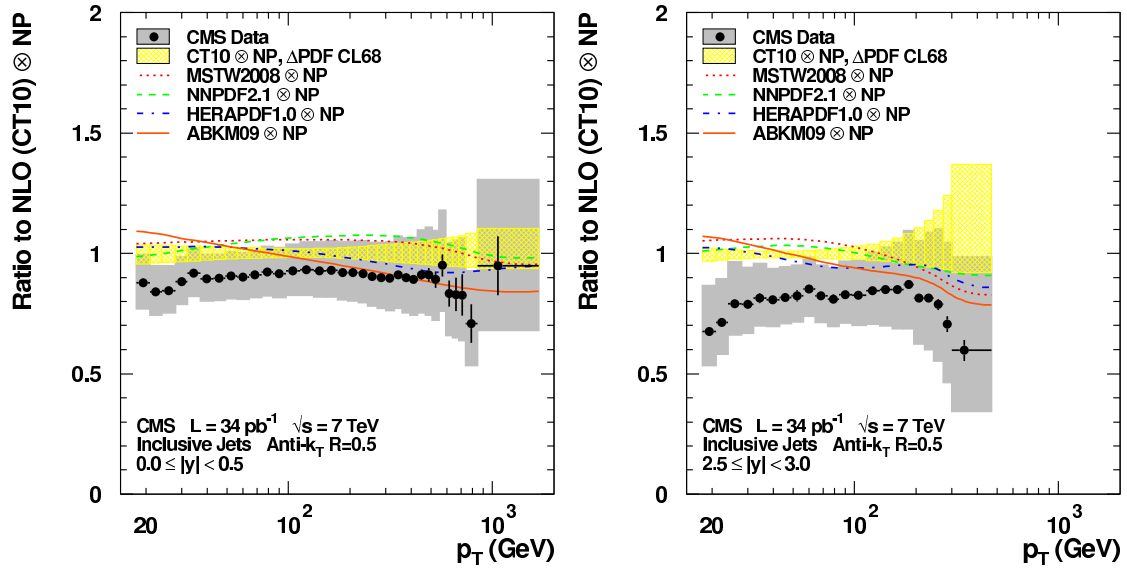


Fig. 49: CMS data on inclusive jet production in central and forward rapidity regions in ratio to the NLO predictions of CT10 and compared to NLO predictions from HERAPDF1.0, ABKM09, MSTW08 and NNPDF2.1

ments are combining their data in order to provide the most complete and accurate set of deep-inelastic data as the legacy of HERA.

Data on inclusive cross-sections have been combined for the HERA-I phase of running and a preliminary combination has been made also using the HERA-II data. This latter exercise also includes the data run at lower proton beam energies in 2007. Combination of $F_2^{c\bar{c}}$ data is underway, and combination of $F_2^{b\bar{b}}$ data and of jet data is foreseen.

The HERA collaborations have used these combined data to determine parton distribution functions (PDFs) in the proton. Because the HERA experiments investigated e^+p and e^-p , charge current(CC) and neutral current (NC) scattering, the inclusive HERA data provide information on flavour separated up- and down-type quarks and antiquarks and on the gluon- from its role in the scaling violations of perturbative quantum-chromo-dynamics. The lower proton beam energy data provide further information on the gluon at small $x \lesssim 0.01$ since they allow a determination of the longitudinal structure function. The charm data provide additional information on heavy quark schemes and heavy quark mass values. The jet data (separate data from H1 and ZEUS at the time of writing) provide additional information on the gluon PDF in the x range, $0.01 \lesssim x \lesssim 0.1$ and on $\alpha_s(M_Z)$.

The analysis of these data sets has resulted in the the HERAPDF parton distribution functions. In this review we have described and compared these sets with each other and with PDF sets from other groups. We have also demonstrated that the HERAPDF sets give successful descriptions of data on W and Z production and on jet production from the Tevatron and the LHC. The currently recommended version of these PDFs, which are available on LHAPDF, are the HERAPDF1.5 NLO and NNLO sets.

References

- [1] V.N Gribov and L.N. Lipatoff 1972 Sov.J.Nucl.Phys.**15** 438
- [2] L.N.Lipatov 1975 Sov.J.Nucl.Phys.**20** 95
- [3] Yu. Dokshitzer 1977 Sov. Phys. JETP **46** 641
- [4] G. Altarelli and G. Parisi 1977 Nucl.Phys B**126** 298
- [5] F. Aaron *et al* (H1 and ZEUS Collaborations) 2010 JHEP **1001** 109
- [6] F. Aaron *et al* (H1 Collaboration) 2009 Eur.Phys.J.C**63** 625
- [7] F. Aaron *et al* (H1 Collaboration) 2009 Eur.Phys.J.C**64** 561
- [8] C. Adloff *et al* (H1 Collaboration) 2000 Eur.Phys.J.C**13** 609
- [9] C. Adloff *et al* (H1 Collaboration) 2001 Eur.Phys.J.C**19** 269
- [10] C. Adloff *et al* (H1 Collaboration) 2003 Eur.Phys.J.C**30** 1
- [11] J. Breitweg *et al* (ZEUS Collaboration) 1997 Phys.Lett.B**407** 432
- [12] J Breitweg *et al* (ZEUS Collaboration) 2000 Phys.Lett.B**487** 53
- [13] J. Breitweg *et al* (ZEUS Collaboration) 1998 Eur.Phys.J.C**7**609
- [14] S. Chekanov *et al* (ZEUS Collaboration) 2001 Eur.Phys.J.C**21**443
- [15] J. Breitweg *et al* (ZEUS Collaboration) 2000 Eur.Phys.J.C**12**411
- [16] S. Chekanov *et al* (ZEUS Collaboration) 2002 Eur.Phys.J.C**28**175

- [17] S. Chekanov *et al* (ZEUS Collaboration) 2002 Phys.Lett.B**539**197
- [18] S. Chekanov *et al* (ZEUS Collaboration) 2004 Phys.Rev.D**70** 052001
- [19] S. Chekanov *et al* (ZEUS Collaboration) 2003 Eur.Phys.J.C**32**1
- [20] A. Benvenuti *et al* (BCDMS Collaboration) 1989 Phys.Lett.B**223** 485
- [21] M. Arneodo *et al et al* (NMC Collaboration) 1997 Nucl.Phys.B**483**3
- [22] A. Aktas *et al* (H1 Collaboration) 2006 Phys.Lett.B**632**35, A.M. Cooper Sarkar *et al* 1999 J.Phys.G, Nucl.Part.Phys.**25**1387, ZEUS-prel-06-003, H1prelim-10-042
- [23] S. Chekanov *et al* (ZEUS Collaboration)2009 Eur.Phys.J.C**61** 223
- [24] H1prelim-09-043
- [25] S. Chekanov *et al* (ZEUS Collaboration)2009 Eur.Phys.J.C**62** 625
- [26] H1prelim-09-042
- [27] S. Chekanov *et al* (ZEUS Collaboration)2010 Eur.Phys.J.C**70** 945
- [28] ZEUS-prel-11-003
- [29] ZEUS-prel-10-017, H1prelim-10-141
- [30] ZEUS-prel-10-018, H1prelim-10-142
- [31] F.D.Aaron *et al* (H1 Collaboration) 2008 Phys.Lett.B**665** 139
- [32] S. Chekanov *et al* (ZEUS Collaboration) 2009 Phys.Lett.B**682** 8
- [33] ZEUS-prel-10-001, H1prelim-10-043
- [34] F.D. Aaron *et al* (H1 Collaboration) 2011 Eur.Phys.J.C**71** 1579
- [35] ZEUS-prel-09-015,H1prelim-09-171
- [36] F.D. Aaron *et al* (H1 Collaboration) 2007 Eur.Phys.J.C**51** 271
- [37] H1prelim-08-074,H1prelim-08-072, H1prelim-08-172
- [38] F.D. Aaron *et al* (H1 Collaboration) 2006 Eur.Phys.J.C**45** 23
- [39] H1prelim-08-173
- [40] S. Chekanov *et al* (ZEUS Collaboration) 2004 Phys.Rev.D**69** 012004
- [41] J. Breitweg *et al* (ZEUS Collaboration) 2000 Eur.Phys.J.C**12** 35
- [42] S. Chekanov *et al* (ZEUS Collaboration)2009 Eur.Phys.J.C**63** 171
- [43] arXiv:0904.3487
- [44] F.D. Aaron *et al* (H1 Collaboration) 2010 Eur.Phys.J.C**65** 89
- [45] S. Chekanov *et al* (ZEUS Collaboration) 2010 Eur.Phys.J.C**65** 65
- [46] H1prelim-11-034,ZEUS-prel-11-001

- [47] F.D. Aaron *et al* (H1 Collaboration) 2010 Eur.Phys.J.C**65** 363
- [48] F.D. Aaron *et al* (H1 Collaboration) 2010 Eur.Phys.J.C**67** 1
- [49] S. Chekanov *et al* (ZEUS Collaboration) 2002 Phys.Lett.B**547** 164
- [50] S. Chekanov *et al* (ZEUS Collaboration) 2007 Nucl.Phys.B**765** 1
- [51] ZEUS-prel-10-008, H1prelim-10-044
- [52] ZEUS-prel-10-009, H1prelim-10-045
- [53] H1prelim-11-042,ZEUS-prel-11-002
- [54] H1prelim-11-143,ZEUS-prel-11-010
- [55] K. Kovarik *et al* 2011 AIP.Conf.Proc.**1369** 80
- [56] A. Accardi *et al* 2011 Phys.Rev.D**84** 014008
- [57] A.M. Cooper-Sarkar *et al* 1988 Phys.C**39** 281
- [58] S. Moch, J.A.M. Vermaseren and A. Vogt 2004 Nucl. Phys. B**688** 101, Nucl. Phys. B**691** 129
- [59] M. Botje QCDNUM 2010 arXiv:1005.1481
- [60] W. Furmanski and R. Petronzio 1982 Z. Phys. C**11** 293
- [61] W.L. van Neerven and E.B. Zijlstra 1991 Phys. Lett. B**272** 127 E.B. Zijlstra and W.L. van Neerven 1991 Phys. Lett. B**273** 476 E.B. Zijlstra and W.L. van Neerven 1992 Phys. Lett. B**297** 377 J. Sanchez Guillen *et al* 1991 Nucl. Phys. B**353** 337
- [62] R.S. Thorne and R.G. Roberts 1998 Phys. Rev. D**57** 6871
- [63] R.S. Thorne 2006 Phys. Rev. D**73** 054019
- [64] R.S. Thorne 2008 private communication.
- [65] A.D. Martin *et al* 2009 Eur.Phys.J.C**63** 189
- [66] P.M. Nadolsky *et al* 2008 Phys.Rev.D**78** 013004
- [67] M. Kramer, F. I. Olness, and D. E. Soper 2000 Phys.Rev.D**62** 096007
- [68] R. Devenish and A. Cooper-Sarkar, *Deep Inelastic Scattering*, Oxford University Press, 2004, Ch. 6.
- [69] R. Devenish and A. Cooper-Sarkar, *Deep Inelastic Scattering*, Oxford University Press, 2004, Ch. 9.
- [70] ZEUS-prel-10-019, H1prelim-10-143
- [71] R.S. Thorne, arXiv:1201.6180
- [72] Wu-Ki Tung *et al* 2007 JHEP **0702** 053
- [73] F. Caola and S. Forte 2008 Phys.Rev.Lett.**101**022001
- [74] Z. Nagy 2002 Phys.Rev.Lett.**88** 122003

- [75] T. Kluge, K. Rabbertz and M. Wobisch, hep-ph/0609285
- [76] S. Chekanov *et al* 2005 Eur.Phys.J.C**42** 1
- [77] P. Nadolsky *et al* 2008 Phys.Rev.D**78** 013004
- [78] H.L. Lai *et al* 2010 Phys.Rev.D**82** 074024
- [79] R.D. Ball *et al* 2008 Nucl.Phys.B**706** 137
- [80] R.D. Ball *et al* 2010 Nucl.Phys.B**849** 296
- [81] S. Alekhin *et al* 2010 Phys.Rev.D**81** 014032
- [82] P. Jimenez-Delgado and E. Reya 2009 Phys.Rev.D**79** 074023
- [83] S. Alekhin *et al*, arXiv:1101.0536
- [84] J. Pumplin 2010 Phys.Rev.D**82** 114020
- [85] J.F.Owens *et al* 2009 AIP Conf.Proc.**1189** 263
- [86] S. Alekhin *et al* 2011 Eur.Phys.J.C**71** 1723
- [87] R.S. Thorne and G. Watt 2011 JHEP **1108** 100
- [88] S. Alekhin *et al* arXiv:1105.5349
- [89] A. D. Martin *et al* 2009 Eur.Phys.J.C**64** 653
- [90] S. Lionetti *et al* 2011 Phys.Lett.**B701** 346
- [91] J. Rojo *et al.* 2010 PoS **DIS2010** 173
- [92] R. Devenish and A. Cooper-Sarkar, *Deep Inelastic Scattering*, Oxford University Press, 2004, Ch. 4.
- [93] S. Alekhin and S. Moch, arXiv:1107.0469
- [94] T. Altonen *et al* (CDF Collaboration) 2009 Phys.Rev.Lett.**102** 181801
- [95] T. Altonen *et al* (CDF Collaboration) 2010 Phys.Lett.B**692** 232
- [96] V.M. Abuzov *et al* (D0 Collaboration) 2008 Phys.Rev.Lett.**101** 062001
- [97] A. Abulencia *et al* (CDF Collaboration) 2007 Phys.Rev.D**75**092006
- [98] G. Aad *et al* (ATLAS Collaboration) arXiv:1109.5141
- [99] G. Aad *et al* (ATLAS Collaboration) arXiv:1203.4051
- [100] CMS Collaboration, CMS-PAS-EWK-11-005
- [101] G. Aad *et al* (ATLAS Collaboration) arXiv:1112.6297
- [102] S. Chatrchyan *et al* (ATLAS Collaboration) 2011 Phys.Rev.Lett.**107** 132001

ZEUS

